

1 **Influence of lateral heterogeneities on strike-slip faults**  
2 **behavior: Insights from analogue models.**~~Strike-slip~~  
3 ~~faulting affecting vertical domains of contrasting brittle~~  
4 ~~strength in the upper crust: Insights from analogue~~  
5 ~~models.~~

6 Sandra González-Muñoz<sup>1</sup>, Guido Schreurs<sup>2</sup>, Timothy C. Schmid<sup>2</sup>, Fidel Martín-  
7 González<sup>1</sup>

8 <sup>1</sup>Área de Geología - ESCET, TECVOLRISK Research Group, Universidad Rey Juan Carlos. C/Tulipan  
9 s/n, Mostoles, 28933 Madrid, Spain

10 <sup>2</sup> Institute of Geological Sciences, University of Bern, Bern, Switzerland

11 *Correspondence to:* Sandra González Muñoz ([sandra.gonzalezmu@urjc.es](mailto:sandra.gonzalezmu@urjc.es))

12  
13  
14 **Abstract**

15 This study investigates ~~how lithological changes can affect how the~~ strike-slip faults ~~propagate across~~  
16 ~~vertical domains of contrasting brittle strength~~ propagation patterns using analogue models. Strike-slip fault  
17 ~~zones~~ are long structures that ~~may~~ cut across pre-existing tectonic or lithological steep boundaries ~~in the~~  
18 ~~upper crust.~~ How strike-slip faulting is affected by a laterally heterogeneous upper crust ~~The interaction~~  
19 ~~between strike slip faulting and these domains~~ is crucial for understanding the evolution of regional and  
20 local fault patterns, ~~potential~~ stress reorientations, and seismic hazard ~~assessment~~. Our models undergo  
21 sinistral distributed strike-slip shear (simple shear) ~~and~~ ~~nd~~ have been analyzed by Particle Image  
22 ~~Velocimetry (PIV).~~ ~~comprise brittle vertical domains with contrasting properties.~~ We use quartz sand and  
23 microbeads as brittle analogue materials over a viscous mixture to distribute the deformation through the  
24 model. ~~We apply Particle Imaging Velocimetry (PIV) and use incremental vorticity to analyse models~~

25 ~~surfaces.~~ The first models investigate strike-slip faulting kinematics with only one brittle material in a  
26 homogeneous upper crust by using ~~-(quartz sand or microbeads) only,~~ simulating a homogeneous crust.  
27 Three further models examine how the presence of a central section which laterally differs in its  
28 properties ~~orientation of a central vertical domain, having a strength contrast with respect to the surrounding~~  
29 ~~domains,~~ influences strike-slip faulting. influences strike-slip faulting. The main observations of this study  
30 are the following:

- 31 • ~~The homogeneous upper crust shows typical Mohr-Coulomb strike-slip faults, with synthetic fault~~  
32 ~~strikes related to the angle of internal friction of the material used~~
- 33 • ~~The heterogeneity upper crust has a profound effect on synthetic fault propagation, interaction and~~  
34 ~~linkage as well as the kinematic evolution of antithetic faults that rotate around a vertical axis.~~
- 35 • ~~The presence of vertical domains of contrasting brittle mechanical strength has a profound effect~~  
36 ~~on synthetic fault propagation, interaction and linkage as well as the kinematic evolution of~~  
37 ~~antithetic faults that rotate about a vertical axis due to the applied simple shear.~~
- 38 • ~~The orientation of the central domain section determines whether antithetic fault activity~~  
39 ~~concentrates along the entire length of the central contact the entire width of the domain boundaries~~  
40 ~~or not. In the first case, fault activity is compartmentalized segmented or the number of different~~  
41 ~~faults formed is increased in distinct domains. In the second case (no or partial fault activity along~~  
42 ~~domain boundaries), the properties of the central material relative brittle strength contrast~~  
43 ~~determines fault propagation, interaction and/or linkage across the central domain.~~
- 44 • ~~These findings have potential implications for nature have been seen in the NW Iberian Peninsula.~~  
45 ~~In this area the change of direction of the sinistral faults and the position of the antithetic faults~~  
46 ~~can be explained due to lithological change.~~

47  
48 ~~These findings were compared with the intraplate fault systems of the NW Iberian Peninsula, which shows~~  
49 ~~synthetic and antithetic faults whose distribution is similar to those observed in our models.~~

## 50 **Keywords**

51 Strike-slip fault zone, Fault interaction, Fault linkage, ~~Vertical brittle strength contrasts~~ Mechanical strength  
52 ~~contrast~~, Analogue modelling

Con formato: Fuente: (Predeterminada) Times New Roman, 10 pto

Con formato: Fuente: (Predeterminada) Times New Roman, 10 pto

Con formato: Fuente: (Predeterminada) Times New Roman, 10 pto

Con formato: Sangría: Izquierda: 0 cm

53

54 **1. Introduction**

55 Strike-slip fault systems in nature extend from a few meters to several hundred kilometers and typically  
56 have complex geometries consisting of separate fault segments offset from each other or comprising  
57 anastomosing, linked faults (e.g., Aydin and Nur, 1982; Barka and Kadinsky-Cade, 1988; Wesnousky,  
58 1988; Stirling et al., 1996; Kim et al., 2004). The evolution of strike-slip fault systems has been studied  
59 in numerous studies focused on the process of offset formation and therefore, basin development,  
60 change of fault polarity and parameters controlling segmentation (e.g., Riedel, 1929; Anderson, 1951;  
61 Deng et al., 1986; Sylvester, 1988; Dooley and Schreurs, 2012; Hatem et al., 2017; Lefevre et al.,  
62 2020a; Visage et al., 2023). Understanding strike-slip fault interaction and linkage is important for its  
63 implications on seismic hazard (Petersen et al., 2011; Bullock et al., 2014), in terms of dynamics, fault  
64 growth and size of earthquakes (e.g. Aki, 1989; Harris and Day, 1999; Scholz, 2002; Wesnousky, 2006;  
65 Shaw and Dieterich, 2007; de Joussineau and Aydin, 2009; Preuss et al., 2019); but also in terms of  
66 regional stress orientations (Kirkland et al., 2008) and in view of the location of geothermal and  
67 hydrocarbon resources (e.g. Sibson, 1985; Martel and Peterson, 1991; Aydin, 2000; Odling et al.,  
68 2004; Cazarin et al., 2021).

69 How faults interact or link is considered to be a function of loading, stress disturbances, rheology and  
70 the geometry of pre-existing structures (e.g., Kim et al., 2004; Myers and Aydin, 2004; Peacock and  
71 Sanderson, 1991, 1992; Burgmann and Pollard, 1994; Sibson, 1985; Gamond, 1983; Rispoli, 1981;  
72 Wesnousky, 1988). Various studies have investigated the influence of vertical changes in upper crustal  
73 strength (e.g. a horizontal sedimentary sequence comprising layers or bodies of different strengths) on  
74 strike-slip fault orientation, segmentation, linkage, and displacement. These studies used field  
75 observations, combined with analytical and numerical methods (e.g. Du and Aydin, 1995; Aydin and  
76 Berryman, 2010; De Dontney et al., 2011), or analogue models (Richard, 1991; Richard et al., 1995;  
77 Gomes et al., 2019; Gabrielsen et al., 2023; Venancio and Alves Da Silva, 2023). However, it is also  
78 important to consider the evolution of strike-slip fault systems in a laterally heterogeneous upper crust.  
79 Strike-slip faults often extend laterally over considerable distances and are thus expected to be  
80 influenced by steeply oriented pre-existing tectonic or lithological boundaries having rocks with  
81 contrasting strength on either side. Such (sub)vertical contacts often occur at terrane boundaries or

**Con formato:** Fuente: (Predeterminada) Times New Roman, 10 pto

**Con formato:** Normal, Sangría: Izquierda: 0,63 cm, Sin viñetas ni numeración

**Con formato:** Fuente: (Predeterminada) Times New Roman, 10 pto, Inglés (Reino Unido)

**Con formato:** Sangría: Izquierda: 0,63 cm, Espacio Antes: 12 pto, Después: 8 pto, Interlineado: Doble

**Con formato:** Fuente: (Predeterminada) Times New Roman, 10 pto

82 within crustal blocks comprising rock units with contrasting strengths, e.g. a magmatic body with steep  
83 margins that intruded into a sedimentary sequence. To our knowledge no modelling studies have yet  
84 investigated how strike-slip fault systems are affected by steeply dipping contacts separating different  
85 rock types. Here we use scaled analogue model experiments analysed by Particle Imaging Velocimetry  
86 (PIV) to assess the role of vertically oriented domains of contrasting brittle strength in the upper crust  
87 on fault kinematics in distributed strike-slip shear. The models were inspired by the deformation pattern  
88 of the NW Iberian Peninsula, which has undergone sinistral shearing during the Alpine Orogeny (e.g.  
89 Martínez Catalán, 2011; Vergés et al., 2019). This particular area shows a system of sinistral faults that  
90 cross lithological domains with contrasting properties and part of their segmentation is conditioned by  
91 these domains. The structural styles and the factors that control the geometry of strike-slip faults have  
92 been investigated in detail in many studies (e.g., Riedel, 1929; Anderson, 1951; Deng et al., 1986;  
93 Sylvester, 1988; Dooley and Schreurs, 2012; Hatem et al., 2017; Lefevre et al., 2020a; Visage et al.,  
94 2023). In nature, strike-slip fault systems typically have complex architectures consisting of numerous  
95 segments separated by steps or of anastomosing, linked fault zones (e.g., Aydin and Nur, 1982; Barka  
96 and Kadinsky-Cade, 1988; Wesnousky, 1988; Stirling et al., 1996; Kim et al., 2004). How faults  
97 interact or link is considered to be a function of loading, stress disturbances, rheology and the geometry  
98 of pre-existing structures (e.g., Kim et al., 2004; Myers and Aydin, 2004; Peacock and Sanderson,  
99 1991, 1992; Burgmann and Pollard, 1994; Sibson, 1985; Gamond, 1983; Rispoli, 1981; Wesnousky,  
100 1988).

Con formato: Fuente: (Predeterminada) Times New Roman, 10 pto

Con formato: Fuente: (Predeterminada) Times New Roman, 10 pto, Inglés (Reino Unido)

Con formato: Fuente: (Predeterminada) Times New Roman, 10 pto

102 Understanding strike-slip fault interaction and linkage is important not only in view of the location of  
103 geothermal and hydrocarbon resources (e.g. Sibson, 1985; Martel and Peterson, 1991; Aydin, 2000;  
104 Odling et al., 2004; Cazarin et al., 2021) but also for its implications on regional stress orientations  
105 (Kirkland et al., 2008), as well as seismic hazard (Petersen et al., 2011; Bullock et al., 2014), in terms  
106 of dynamics, fault growth and size of earthquakes (e.g. Aki, 1989; Harris and Day, 1999; Scholz, 2002;  
107 Wesnousky, 2006; Shaw and Dieterich, 2007; de Jossineau and Aydin, 2009; Preuss et al., 2019).

Con formato: Sangría: Izquierda: 0,63 cm

108 Various studies have investigated the influence of vertical changes in mechanical strength (e.g., a  
109 horizontal sedimentary sequence comprising layers or bodies of different strengths) on strike-slip fault  
110 orientation, segmentation, linkage, and displacement, using field observations, combined with

analytical and numerical methods (e.g. Du and Aydin, 1995; Aydin and Berryman, 2010; De Dontney et al., 2011), or analogue models (Richard, 1991; Richard et al., 1995; Gomes et al., 2019; Gabrielsen et al., 2023; Venancio and Alves Da Silva, 2023).

Strike-slip fault systems have large aspect ratios (i.e., ratio of length vs width) and can extend over hundreds or even thousands of kilometres and often cut across pre-existing tectonic or lithological boundaries that are steeply oriented and have rocks of contrasting mechanical strength on either side. Hence, it is also important to understand the interaction between vertical domains of contrasting mechanical strength and strike slip faulting. To our knowledge no modelling studies have systematically investigated how strike slip fault systems are influenced by pre-existing steeply oriented domains with rocks of contrasting mechanical strength on either side of the contacts. Such (sub)vertical contacts often occur at crustal terrane boundaries, but also occur within crustal blocks comprising rock units of contrasting strength separated by vertical boundaries, e.g. a magmatic body with steep margins that intruded into a sedimentary sequence.

Here we use scaled analogue model experiments analysed by PIV to assess the role of vertical domains of contrasting brittle strength in the upper crust on fault kinematics in distributed strike slip shear. Our results show that the presence of such vertical domains with different strengths has a profound influence on the kinematic evolution of strike slip fault systems. We compare our experimental model results with a crustal scale example in the NW part of the Iberian Peninsula, where two large parallel and sinistral strike slip fault systems cut lithological domains of contrasting strength.

## 2. Methods

### 2.1. Analogue model setup

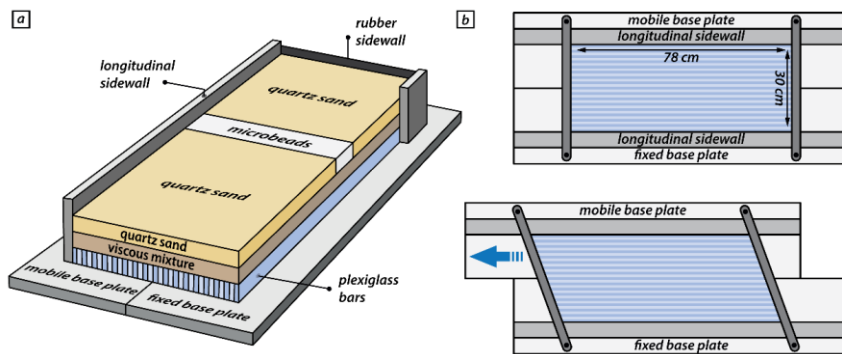
The experimental set-up for simulating distributed strike-slip shear included a mobile base plate that could be translated horizontally ~~past~~<sup>above</sup> a fixed base plate (Fig. 1). An assemblage of 60 individual and moveable plexiglass bars (each 78 cm long, 5 cm high and 5 mm wide) was positioned on top of two base plates. The assemblage of plexiglass bars was confined by carbon-fiber sidewalls on the long sides (Fig. 1b) and wooden bars (c. 5 mm high, 2 cm wide and 40 cm long) on the short sides (Fig. 1b, c), that could pivot below the longitudinal sidewalls. The model was constructed on top of the plexiglass bars and

Con formato: Sangría: Izquierda: 0,63 cm,  
Espacio Antes: 12 pto, Después: 8 pto,  
Interlineado: Doble

139 consisted of a 2 cm-thick viscous layer, simulating the ductile lower crust, overlain by a 2 cm-thick layer  
 140 of granular materials simulating the brittle upper crust. The short sides of the model were confined by  
 141 vertical rubber sheets. Although our model set-up ~~thus~~ included both a horizontal viscous layer overlain by  
 142 a horizontal brittle layer, our experiments focus on the influence of vertical domains with brittle strength  
 143 contrasts on strike-slip faulting. The function of the viscous layer, directly overlying the plexiglass bars, is  
 144 to distribute the applied shear deformation over the entire width of the model in the overlying brittle layer  
 145 (e.g. Schreurs, 1991, 2003; Dooley and Schreurs, 2012).

146 Each model had an initial rectangular shape in map view, with a length of 78 cm parallel to the shear  
 147 direction and a width of 30 cm perpendicular to it. The movement of the mobile base plate occurred by  
 148 computer-controlled stepper motors at a constant velocity of 40 mm/h, resulting in 80 mm of total  
 149 displacement after two hours. Displacement of the mobile base plate changed the initial rectangular shape  
 150 of the overlying assemblage of plexiglass bars into a parallelogram simulating simple shear.

151



152

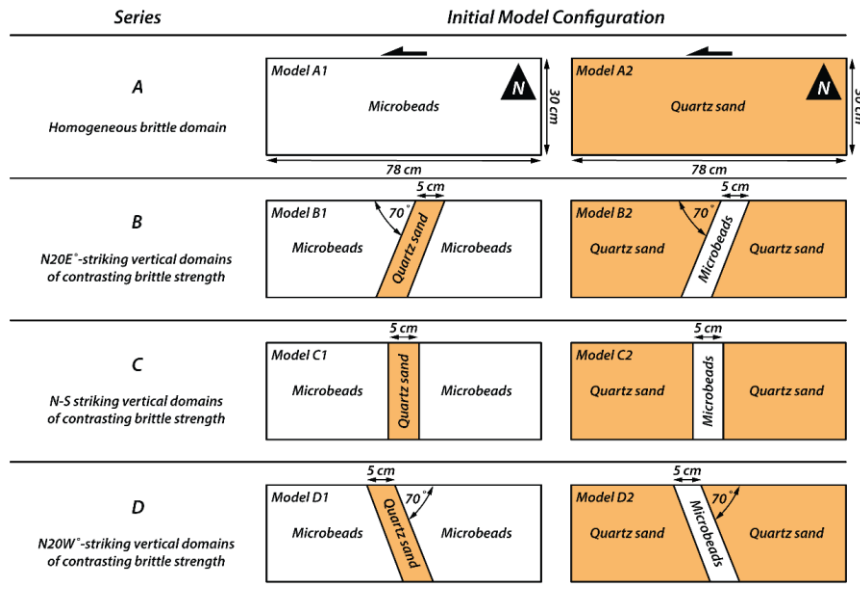
153 **Figure 1: Schematic experimental setup.** (a) The base of the model set-up consists of a fixed plate and a mobile  
 154 plate overlain by an assemblage of individual and moveable plexiglass bars. The model is constructed on top of  
 155 the plexiglass bars and is confined by two longitudinal sidewalls and two short sidewalls consisting of rubber  
 156 sheets. (b) upper panel: Initial position of base plates overlain by plexiglass bars confined on the short sides by  
 157 wooden bars that can pivot about a vertical axis; lower panel: Sinistral horizontal displacement of the mobile  
 158 base plate induces a simple shear movement in the overlying assemblage of plexiglass bars as they slide past one  
 159 another.

160

161 We performed four series of simple shear experiments, referred to as Series A, B, C and D (Fig. 2). Series  
 162 A involved two ~~reference~~ models with only one brittle material (Fig. 2a), ~~either quartz sand or~~

163 ~~microbeads~~quartz sand or microbeads, to investigate strike-slip fault kinematics ~~in-in~~ a homogeneous upper  
164 crust, without any lateral variations in mechanical strength. In the ~~subsequent~~other three series (Fig. 2b-d),  
165 we introduced ~~vertical domain boundaries across which the mechanical strength varied laterally~~vertical  
166 ~~domains that consisted of quartz sand or microbeads~~. Each model had three domains with a ~~e~~ 5-cm-wide  
167 central domain consisting of a different ~~brittle~~ material than the domains on either side. The difference  
168 between Series B, C and D is the orientation of the central domain with respect to the shear direction, ~~which~~  
169 ~~changed from one series to the next~~. To achieve such a model set-up, two vertical thin sheets of cardboard  
170 (< 1 mm) were first placed as provisional walls, spaced 5 cm apart, on top of the viscous layer in the central  
171 domain of the model, parallel to the required orientation of the vertical domain boundaries. Subsequently,  
172 the different granular materials were sieved on top of the viscous layer and once the desired model thickness  
173 was reached, the cardboard sheets were carefully removed. Although removal of the cardboard produced  
174 increased dilation along a narrow zone, it hardly affects the de facto function of this vertical boundary as a  
175 primary surface with materials of contrasting brittle strength on either side. For descriptive purposes, we  
176 defined a North direction, which is perpendicular to the applied shear direction and parallel to the short  
177 sides of the undeformed model (Fig. 2a). In models with a brittle strength contrast, we can distinguish two  
178 outer domains, a western and an eastern one, and a central domain (Fig. 2b-d).

179



180  
 181 **Figure 2: Schematic drawing of the materials used and their surface distribution at the initial stage. All models**  
 182 **have a length of 78 and a width of 30 cm. The references about the patterns observed have been given by using**  
 183 **the long side of the edge of the models as “north”. In the series of models referred as A, only one type of material**  
 184 **(quartz sand or microbeads) has been used. The diagrams of series B, C and D show the position and orientation**  
 185 **of the vertical domain boundaries in plan view and which materials were used. Schematic top views of the four**  
 186 **series of models, with dimensions and brittle analogue materials used**  
 187

## 188 2.2. Analogue materials

189 We used two different types of granular materials in our analogue models to assess the role of vertical zones  
 190 of contrasting mechanical strength in the upper crust: quartz sand and microbeads grains. The quartz sand  
 191 (distributor Carlo Bernasconi AG; [www.carloag.ch](http://www.carloag.ch)) has a grain size between 60 and 250  $\mu\text{m}$  with a bulk  
 192 density of 1560  $\text{kg m}^{-3}$ , whereas the grain size of the microbeads (distributor: Worf Glasskugeln, Germany)  
 193 lies between 150 and 210  $\mu\text{m}$  with a bulk density of 1400  $\text{kg m}^{-3}$ . These density values were achieved by  
 194 sieving the granular material into the model box from a height of 30 cm. Both, quartz sand and microbeads  
 195 deform according to the Coulomb failure criterion and have internal peak friction angles of 36° and 22° and  
 196 cohesion values of  $50 \pm 26$  Pa and  $25 \pm 4$  Pa, respectively (Panien et al., 2016; Schmid et al., 2020). The  
 197 considerable difference in the internal peak friction angle between the two materials makes them suitable  
 198 for simulating contrasting upper crustal rocks. According to their difference in the internal friction angle,  
 199 we consider the microbeads and quartz sand as weak and strong materials, respectively.



200 The viscous layer in our models had a density of  $1600 \text{ kgm}^{-3}$  and consisted of a mixture of SGM-36  
 201 polydimethylsiloxane (PDMS) and corundum sand (weight ratio of 0.965: 1.000). The mixture has a quasi-  
 202 linear viscosity of  $1.5 \times 10^5 \text{ Pa s}$  and a stress exponent of 1.05 (Zwaan et al., 2018). The properties of all  
 203 analogue materials are summarized in Table 1.

204

205

Granular materials	Quartz sand	Microbeads	Viscous material	PDMS/corundum mixture
Density ( $\text{kg/m}^3$ )	1560	1400	Density ( $\text{kg/m}^3$ )	1600
Grain size ( $\mu\text{m}$ )	60-250	150-210	Viscosity ( $\text{Pa s}$ )	$1.5 \times 10^5$
Peak friction coefficient $\mu$ and angle, $\phi$	$0.72 - 36^\circ$	$0.41 - 22^\circ$	Stress exponent n	1.05
Cohesion (Pa)	$50 \pm 26$	$25 \pm 4$		

206 **Table 1:** Materials properties of used granular and viscous materials (after Panien et al., 2006; Schmid et al., 2020).

207

208

### 209 [2.4.2.3. Scaling](#)

210 For brittle Mohr-Coulomb type materials, dynamic similarity is given by the equation for stress ratios

$$\sigma^* = \rho^* g^* h^* \quad (1),$$

211 where  $\rho^*$ ,  $g^*$  and  $h^*$  are the ratios of model to nature for density, gravity and length, respectively. Note,

212 that our two used granular materials have different densities, cohesions and internal friction coefficients.

213 However, the resulting scaling factors are nearly identical and therefore we provide only the scaling factors

214 for quartz sand. Where scaling factors substantially differ, we denote them with subscripts “qtz” and “mb”

215 for quartz sand and microbeads, respectively. Our model setup yields a length scaling factor of  $h^* =$

216  $2 \times 10^{-6}$  and a gravity scaling factor of 1. For quartz sand, the density scaling factor is  $\rho_{qtz}^* \sim 0.6$  and the

217 cohesion factor is  $C_{qtz}^* = 1 \times 10^{-6}$  (using a cohesion of  $\sim 50 \text{ Pa}$  and  $50 \text{ MPa}$  for our quartz sand and upper

218 crustal rocks, respectively; Byerlee, 1978). Additionally, for microbeads the density scaling factor and

219 cohesion scaling factor are  $\rho_{mb}^* \sim 0.5$  and  $C_{mb}^* = 1 \times 10^{-6}$  (assuming a weakened natural rock type with a  
220 cohesion of c. 25 MPa), respectively. Using these scaling factors yields a stress scaling factor of  $\sigma^* =$   
221  $1 \times 10^{-6}$  for both quartz sand and microbeads.

222 Assuming a lower crustal viscosity of  $\eta = 10^{22}$  Pa s (Moore and Parsons, 2015; Zhang and Sagiya, 2017)  
223 yields a viscosity ratio  $\eta^* = 1 * 10^{-17}$  (using the viscosity of  $1.5 * 10^5$  Pa s for the viscous analogue  
224 material).

225 The strain rate ratio is obtained from the stress ratio and the viscosity ratio by (Weijermars and Schmeling,  
226 1986):

$$\dot{\epsilon}^* = \frac{\sigma^*}{\eta^*} \quad (2).$$

227 Note that due to the simple shear setup, we substitute the strain rate scaling factor  $\dot{\epsilon}^*$  with the shear strain  
228 rate scaling factor  $\dot{\gamma}^* = 1 \times 10^{11}$ . Next, the velocity scaling factor  $v^*$  and a time scaling factor  $t^*$  are  
229 calculated with

$$\dot{\gamma}^* = \frac{v^*}{h^*} = \frac{1}{t^*} \quad (3)$$

230 yielding a velocity scaling factor  $v^* = 2 \times 10^5$  and a time scaling factor  $t^* = 1 \times 10^{-11}$ .

231 Based on our scaling, 1 cm in our experiments corresponds to 5 km in nature and the applied velocity of 40  
232 mm h<sup>-1</sup> converts to a velocity of ~2 mm a<sup>-1</sup> in nature. Using the shear strain rate scaling factor  $\dot{\gamma}^*$ , the bulk  
233 shear strain rate  $\dot{\gamma} = 3.7 \times 10^{-5} \text{ s}^{-1}$  in our models translates to a shear strain rate of  $\dot{\gamma} = 3.7 \times 10^{-16} \text{ s}^{-1}$   
234 in nature and 1 h in our analogue experiments translates to ~12.5 Myr in nature.

235 In order to verify dynamic similarity of brittle natural and experimental material we calculate the  
236 Smoluchowski number  $S_m$ , which is the ratio between gravitational stress and cohesive strength (Ramberg,  
237 1981):

$$S_m = \frac{\rho gh}{C + \mu \rho gh} \quad (4),$$

238 where  $\rho$ ,  $h$ ,  $C$  and  $\mu$  are the density, thickness, cohesion, and friction coefficient, respectively of the brittle  
 239 material. With a cohesion of 50 MPa and a friction coefficient of ~0.6 (Byerlee, 1978) for upper crustal  
 240 rocks, this yields values of  $S_m \sim 1$  for our models as well as for nature. We further calculate the Ramberg  
 241 number  $R_m$  to ensure dynamic and kinematic similarities between the viscous layers.

$$R_m = \frac{\rho gh^2}{\eta v} \quad (5)$$

242 For our velocity of 40 mm h<sup>-1</sup>, this yields a Ramberg number of 6 for both, our models and nature. The  
 243 Reynolds number  $R_e$  is defined as the ratio between inertial forces and viscous forces and is for all our  
 244 models as well as for the natural prototype  $\ll 1$ :

$$R_e = \frac{\rho v h}{\eta} \quad (6)$$

245 Based on the applied scaling laws, the material properties and the similar non-dimensional numbers for  
 246 model and nature, we consider our models to be properly dynamically scaled. Model parameters and  
 247 dynamic numbers of the used materials are specified in Table 2.

248

	General parameters			Brittle upper crust		Ductile lower crust		Dimensionless numbers		
	Gravity [m/s <sup>2</sup> ]	Crustal thickness [m]	Shear velocity [m/s]	Density [kg/m <sup>3</sup> ]	Cohesion [Pa]	Density [kg/m <sup>3</sup> ]	Viscosity [Pa s]	Smoluchowski Sm	Ramberg Rm <sup>1</sup>	Reynolds Re
Model	9.81	4 x 10 <sup>-2</sup>	1.1 x 10 <sup>-6</sup>	1560	50	1600	1.5 x 10 <sup>5</sup>	1	6	$\ll 1$
Nature	9.81	2 x 10 <sup>4</sup>	6.3 x 10 <sup>-11</sup>	2700	5 x 10 <sup>7</sup>	2900	1 x 10 <sup>22</sup>	1	6	$\ll 1$
Scaling ratios $x^* = x^m/x^n$ [dimensionless]										
	$\sigma^*$	$\rho^*$	$g^*$	$h^*$	$C^*$	$\gamma^*$	$\eta^*$	$v^*$	$t^*$	
	1 x 10 <sup>-6</sup>	0.5 <sup>1</sup> -0.6	1	2 x 10 <sup>-6</sup>	5 <sup>1</sup> -10 x 10 <sup>-7</sup>	1 x 10 <sup>11</sup>	1 x 10 <sup>-17</sup>	2 x 10 <sup>5</sup>	1 x 10 <sup>-11</sup>	

249 <sup>1</sup> Lower values for scaling factors  $\rho^*$  and  $C^*$  refer to microbeads.

250 **Table 2:** Scaling parameters and scaling factors.

251

252  
253

254  
255  
256

#### 2.5.2.4. Deformation monitoring and quantification

257 Since the experiments were conducted using a simple shear setup, vertical motions during deformation  
258 were negligible, with nearly all movement located within the horizontal plane. The different experiments  
259 were monitored by an automated Nikon D810 (36 MPx) DSLR camera positioned above the experimental  
260 model. Images were taken at fixed intervals of 60 s during two hours, resulting in 121 subsequent top view  
261 images of the model surface. For a quantitative 2D analysis of the surface deformation, we used the  
262 StrainMaster module of the LaVision® DaVis image correlation software. Using a calibration plate, the  
263 software corrects the top view images for lens distortion effects (i.e., unwarping), applies image  
264 rectification and provides a scaling function that maps coordinates from the camera sensor to physical world  
265 coordinates with a resolution of ~9 px/mm. The digital image correlation calculates local displacement  
266 vectors on subsequent images using a square matching algorithm with adaptive multi-pass cross-  
267 correlation. To properly track ~~freckle~~ the grain movement patterns, we sprinkled coffee grains on the model  
268 surface prior to the model run. For each image, the analyzed area is subdivided into small interrogation  
269 window for which a local displacement vector is determined by cross-correlation. We used subsets (i.e.,  
270 interrogation windows) of 31 by 31 pixels with a 75% overlap for the local displacement calculations that,  
271 assembled result in incremental (60 s interval) displacement fields for the horizontal x- and y-components  
272  $u_x$  and  $u_y$ , respectively with a vector resolution of ~1.3 vectors/mm.

273 Postprocessing included an outlier filter to fill gaps of pixels within a 3 by 3 neighborhood (Westerweel  
274 and Scarano, 2005). Discarded vectors in the displacement fields were replaced by an iterative interpolation  
275 requiring at least two neighboring vectors. For quantifying deformation at the model surface, we calculate  
276 the z-vorticity  $\omega_z$  (i.e., a rotation measure in the xy plane a local measure of rotation within the xy plane)  
277 as a proxy for shear movement along strike-slip faults. In our models the X-axis corresponds to the long  
278 side of the rectangle; and the Y-axis corresponds to the short side of the model. In contrast to the shear  
279 strain  $\epsilon_{xy}$ , vorticity is not dependent on the orientation of the coordinate system, which is crucial when  
280 quantifying deformation along faults that strike obliquely with respect to the coordinate system (e.g., Cooke  
281 et al., 2020).  $\omega_z$  can be derived from local displacement gradients according to equation 1:

$$\omega_z = \frac{\partial u_y}{\partial x} - \frac{\partial u_x}{\partial y} \quad (7)$$

282 With  $u_x$  and  $u_y$  being the horizontal displacement components in the x, and y direction, respectively. Due  
283 to convention, positive and negative  $\omega_z$  values refer to sinistral and dextral relative displacement,  
284 respectively. Within the predefined increment of 60 s,  $\omega_z$  values are consistently within the range [-2%,  
285 2%] and we set a threshold of -0.5% and 0.5% to distinguish between active deformation and background  
286 noise for dextral and sinistral shear sense, respectively. In the results section we present  $\omega_z$  at deformation  
287 stages every 30 min (i.e., after 30, 60, 90, and 120 min). Finite deformation after 120 min for each model  
288 is illustrated with a surface photograph and enhanced with superposed line drawings of the fault pattern.  
289 For the statistical analysis of fault orientations, we traced active fault segments (i.e.,  $\omega_z \leq -0.5\%$  or  $\omega_z \geq$   
290  $0.5\%$ ) in MATLAB using polylines, where each fault segment is defined by two consecutive vertices. At  
291 each time step, segment length and azimuth were calculated and visualized in length-weighted rose  
292 diagrams.

293

294

295

296

297

## 298 **4.3. Results**

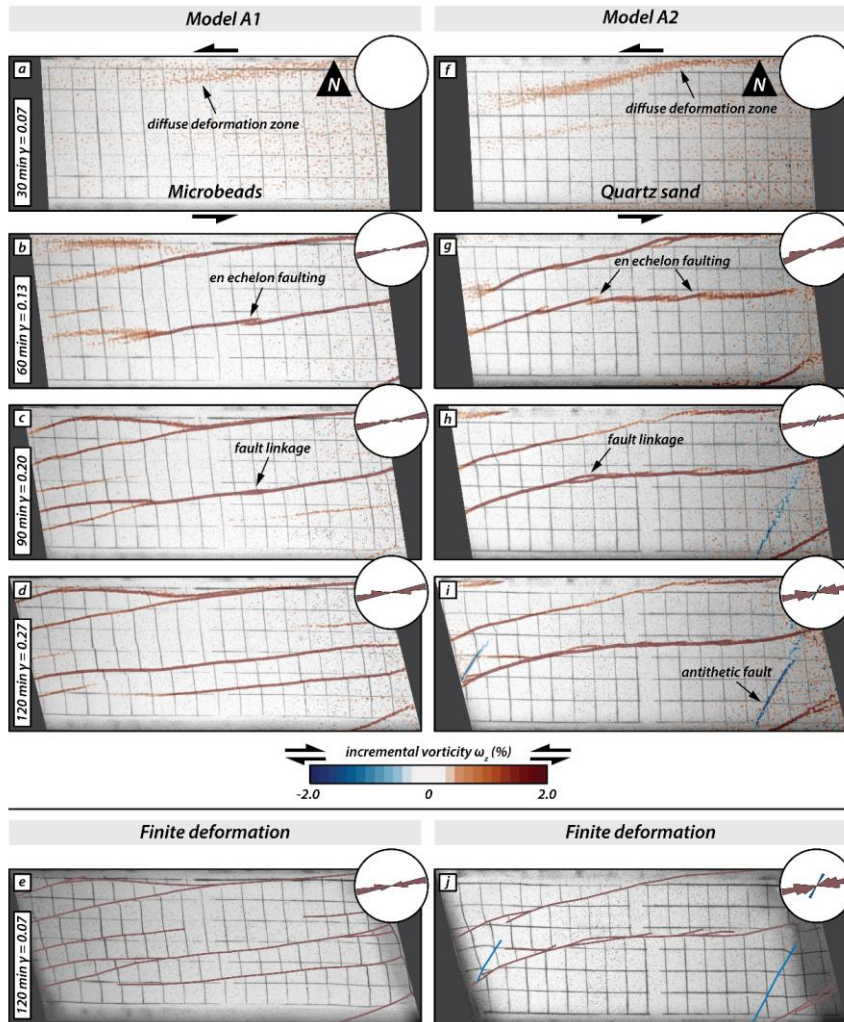
299 We present the results of eight distributed strike slip shear experiments, grouped in four series of two  
300 models each. Series A models included two reference models having a homogeneous upper brittle layer,  
301 whereas Series B, C and D models had vertical domains with contrasting brittle strengths (Fig. 2).

302

### 303 **4.3.3.1. Series A: Fault evolution in a homogeneous upper crust**

304 The Series A models consisted of a homogeneous upper crustal layer composed of either microbeads (Fig.  
305 3; Model A1) or quartz sand (Fig. 3; Model A2). The incremental strain panels document that strain  
306 localized first in the model with quartz sand, while deformation was still diffuse in the model with  
307 microbeads (Fig. 3a and f), i.e. strain localization occurs at lower amounts of applied simple shear in quartz  
308 sand than in microbeads. With progressive sinistral simple shear deformation, slightly overlapping right-  
309 stepping *en echelon* strike-slip faults with a sinistral displacement formed (Fig. 3b and g). These faults were  
310 synthetic with respect to the bulk simple shear. In the model with microbeads (Model A1) the first synthetic  
311 faults had an orientation of  $e-N79^{\circ}E$  (Fig. 3b), whereas in the model with quartz sand (Model A2) their  
312 orientation was  $e-N72^{\circ}E$  (Fig. 3g). Initial deformation in both models is accommodated by synthetic  
313 (sinistral) strike-slip faults ~~only~~ (Fig. 3a, b and f, g). As deformation progressed, individual fault segments  
314 linked up forming major sinistral strike-slip faults (Fig 3c and h). Antithetic faults only developed in Model  
315 A2 (quartz sand only; Fig. 3h and i) at later stages of deformation. These faults were confined in between  
316 previously formed synthetic faults. The final deformation stage (Fig. 3e and j) shows that most deformation  
317 was taken up by major synthetic faults that crossed the entire length of the model. At the final stage, the  
318 initial *en echelon* pattern of faulting was better preserved in the quartz sand model than in the microbeads  
319 model, resulting in a wider damage zone in the former.

320



321

322 Figure 3: Overview of Series A models: Simple shear deformation of two models with a homogenous upper  
 323 brittle layer. The first four panels of each series show surface photographs with the incremental vorticity after  
 324 30 minutes (20 mm displacement of mobile base plate), 60 minutes (or 40 mm displacement), 90 minutes (or 60  
 325 mm displacement) and 120 minutes (or 80 mm displacement). Incremental positive and negative values indicate  
 326 sinistral (synthetic, red) and dextral (antithetic, blue) relative movement, respectively. The last panel for each  
 327 series shows a surface photograph of the final stage overlain with the interpreted fault pattern; red lines are  
 328 sinistral faults, blue lines are dextral faults.

329

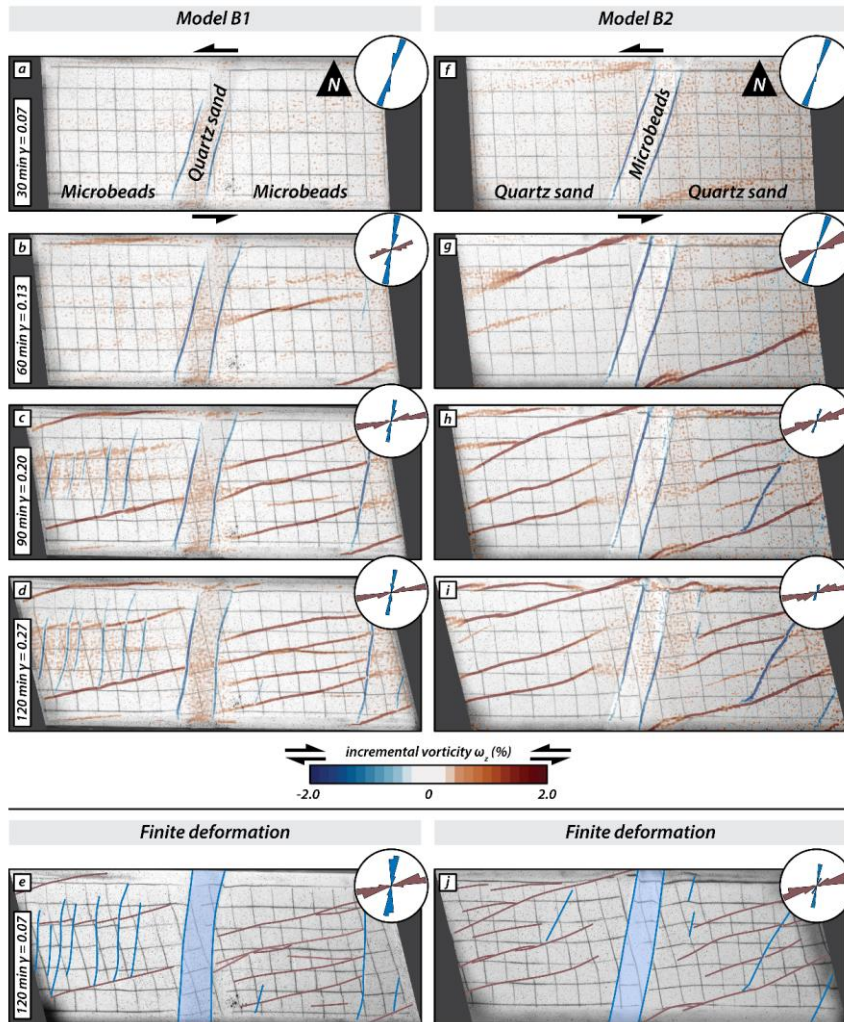
330

331

332 **4.4.3.2. Series B: Fault evolution in models with N20°E vertical domain boundaries**

333 The vertical domain boundaries in the Series B models were oriented N20°E. Model B1 had a central  
334 domain consisting of strong quartz sand with weak microbeads in the adjacent, western and eastern domains  
335 (Fig. 4; Model B1), whereas in Model B2 it was the other way around. (Fig. 4; Model B2). Both models  
336 showed the development of dextral strike-slip (antithetic, with respect to sinistral simple shearing) faults  
337 along the vertical boundaries of the central domain (Fig. 4a, f). ~~Slightly later~~Later, sinistral strike-slip faults  
338 (synthetic) formed in the western and eastern domains (4b, g). Although these faults propagated laterally  
339 with time, none of the synthetic faults crossed the central domain. Instead, they halted at or close to the  
340 boundary faults along the central domain (Fig. 4c, h). In Model B1 a few antithetic faults formed in between  
341 pre-existing synthetic faults in ~~the outer~~the western and eastern domains, striking at c. N60°E (Fig. 4d, e).  
342 Antithetic faults developed also in the western and eastern domains of Model B2, almost coevally with the  
343 synthetic faults. They strike at higher angles to the shear direction than those antithetic faults confined  
344 between overlapping synthetic faults in Model B2. With increasing deformation, the central domain and its  
345 bordering antithetic faults rotated counterclockwise in both models (Fig. 4a-e, f-j), as did the antithetic  
346 faults in the western and eastern domains, which acquired a slight sigmoidal ~~“S-shaped”~~shape form (e.g.  
347 Fig. 4j)





348

349 **Figure 4: Overview of Series B models: Simple shear deformation of two models with vertical domains of**  
 350 **contrasting brittle strength oriented N20°E. The first four panels of each series show surface photographs with**  
 351 **the incremental vorticity after 30 minutes (20 mm displacement of mobile base plate), 60 minutes (or 40 mm**  
 352 **displacement), 90 minutes (or 60 mm displacement) and 120 minutes (or 80 mm displacement). Incremental**  
 353 **positive and negative values indicate sinistral (synthetic, red) and dextral (antithetic, blue) relative movement,**  
 354 **respectively. The last panel for each series shows a surface photograph of the final stage overlain with the**  
 355 **interpreted fault pattern; red lines are sinistral faults, blue lines are dextral faults.**

356

357

358

359

360

361

#### 4.6.3.3. Series C: Fault evolution in models with N-S vertical domain boundaries

362

363

364

365

366

367

368

369

370

371

372

373

374

375

376

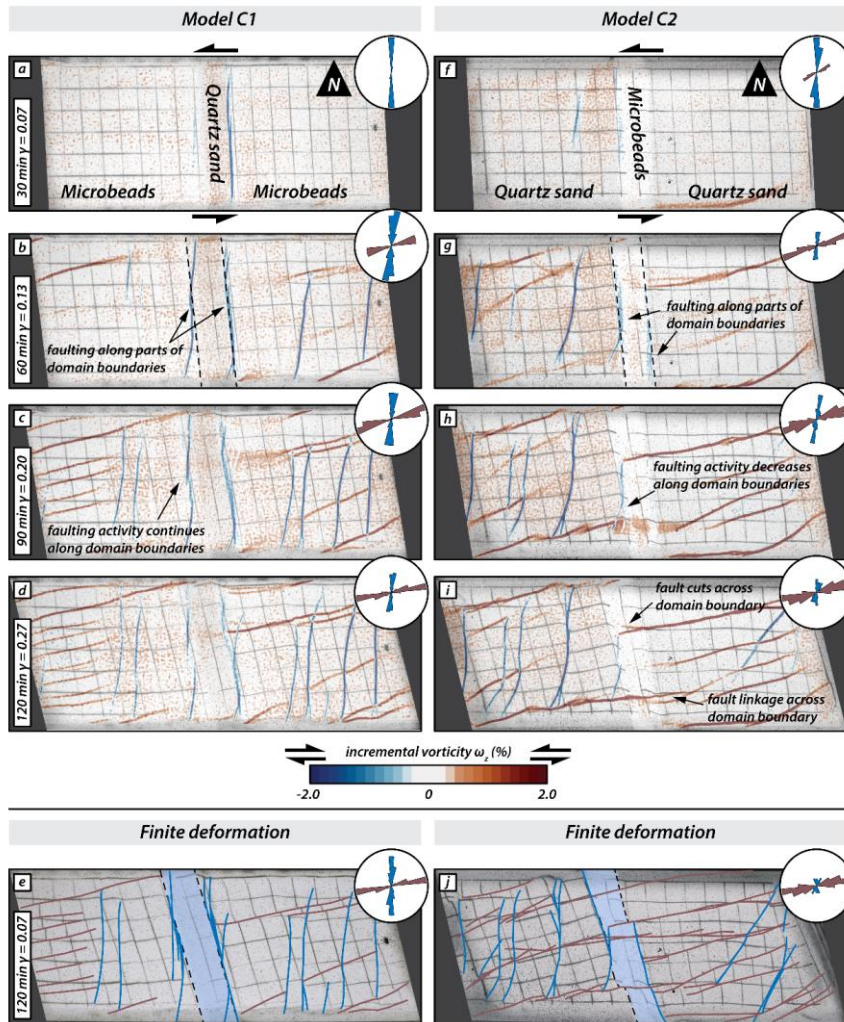
377

378

379

380

~~The Series C models had vertical N-S striking domain boundaries. Model C1 had a 5 cm wide central domain of quartz sand with microbeads on either side (Fig. 5; Model C1), whereas in Model C2 it was the other way around (Fig. 5; Model C2).~~ During the early stages of simple shear, dextral (antithetic) faults formed along the N-S striking borders of the central domain (Fig. 5b, g) in both models, but earlier and more pronounced in Model C1. With progressive shearing, both synthetic and antithetic faults formed in the outer domains of both models (Fig. 5c and h). In Model C2, activity along the antithetic faults bordering the central domain ceased, and synthetic faults propagated from the outer domains into the central weak domain (Fig. 5h-j). In contrast, in Model C1, the antithetic faults along the borders of the central domain remained active, and no synthetic faults crossed the central strong domain (Fig. 5d). In the eastern domain of Model C2, a few antithetic faults formed in between major synthetic faults, striking at a lower angle to the shear direction than earlier formed antithetic faults in the western domain. With progressive simple shear the central domain showed counterclockwise rotation ~~about around~~ a vertical axis in both models and antithetic faults obtained a sigmoidal shape ~~as seen~~ in top view (Fig. 5i). As the initial N-S antithetic faults bordering the central domain rotated counterclockwise, activity along these faults ~~diminished-stopped~~ and ~~new fault segments parallel to earlier antithetic faults formed in the western and eastern domains~~ ~~new fault segments appeared striking nearly parallel to earlier formed antithetic faults in the western and eastern domain~~ (Fig. 5d, e). At the final stage of Model C2, antithetic faults dominated in the western domain and synthetic faults in the eastern domain. In contrast, in Model C1, ~~both~~ antithetic and synthetic faults were present in both the western and eastern domain.



381

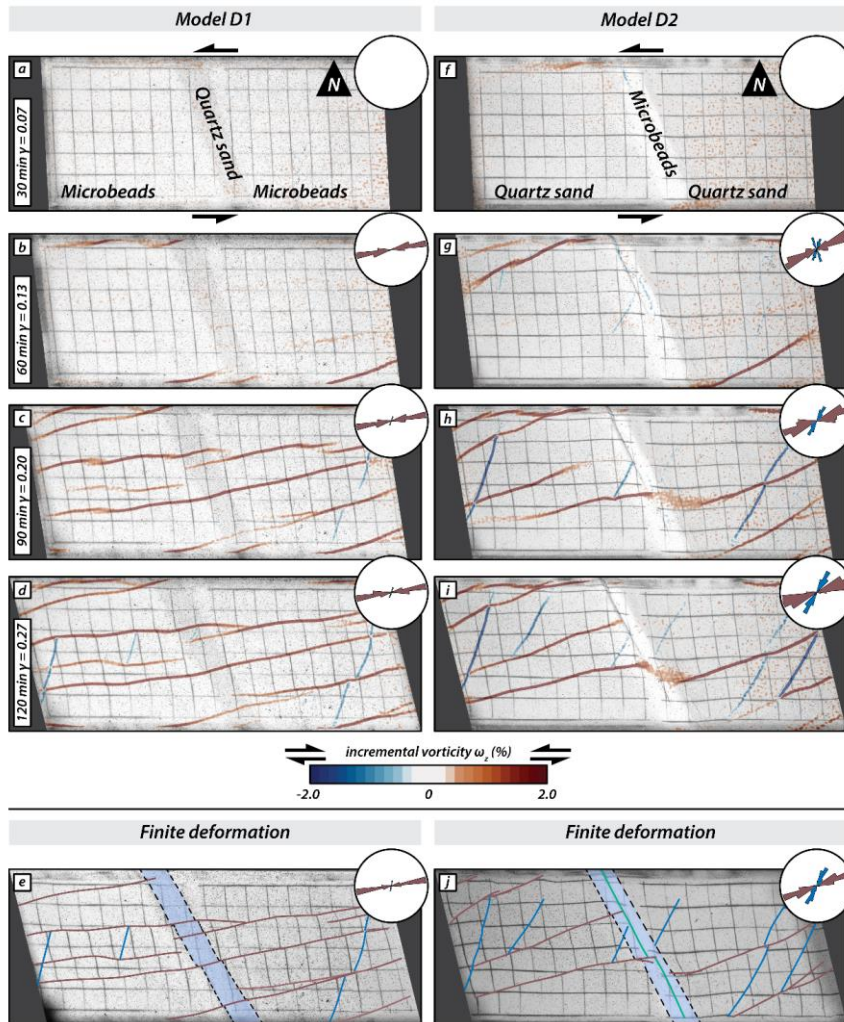
382 Figure 5: Overview of Series C models: Simple shear deformation of two models with vertical domains of  
 383 contrasting brittle strength striking N-S. The first four panels of each series show surface photographs with the  
 384 incremental vorticity after 30 minutes (equivalent to 20 mm displacement of the mobile base plate), 60 minutes  
 385 (or 40 mm displacement), 90 minutes (or 60 mm displacement) and 120 minutes (or 80 mm displacement).  
 386 Incremental positive and negative values indicate sinistral (synthetic, red) and dextral (antithetic, blue) relative  
 387 movement, respectively. The last panel for each series shows a surface photograph of the final stage overlain by  
 388 the interpreted fault pattern; red lines are sinistral faults, blue lines are dextral faults.

389

390

391 **4.7.3.4. Series D: Fault evolution in models with N20°W striking vertical domain boundaries**

392 ~~In the series D models the orientation of the vertical central domain was N20°W. In Model D1 the central~~  
393 ~~domain consisted of a 5 cm wide central band of quartz sand with microbeads on either side (Fig. 6; Model~~  
394 ~~D1), whereas in Model D2 it was the other way around (Fig. 6; Model D2).~~ In contrast to the Model C  
395 series, no faults formed along the boundaries of the central domain in both Models D1 and D2 (Fig. 6a and  
396 f). Model D1 is dominated by synthetic faults crosscutting the central strong domain (6c-e). As these faults  
397 traversed the central domain, they slightly changed their strike-orientation. In contrast, in Model D2 the  
398 weak microbeads of the central domain were internally deformed and oblique-slip reverse faults formed,  
399 which propagated laterally and parallel to the domain boundaries (Fig. 6g-j). Synthetic faults formed both  
400 in the western and eastern domain of Model D2, while antithetic faults formed later and in between  
401 overlapping synthetic faults (Fig. 6g-j). With progressive deformation synthetic faults from the western and  
402 eastern domain in Model D2 propagated partially into the central, weak central domain, but halted at the  
403 previously formed oblique-slip reverse faults (Fig. 6h and i). During late stages of deformation a few  
404 antithetic faults formed in Model D1 in between earlier formed synthetic faults, striking at somewhat larger  
405 angles to the shear direction than in Model D2.



406

407 Figure 6: Overview of Series D models: Simple shear deformation of two models with N20°W striking vertical  
 408 domains of contrasting brittle strength. The first four panels of each series show surface photographs with the  
 409 incremental vorticity after 30 minutes (20 mm displacement of mobile base plate), 60 minutes (or 40 mm  
 410 displacement), 90 minutes (or 60 mm displacement) and 120 minutes (or 80 mm displacement). Incremental  
 411 positive and negative values indicate sinistral (synthetic, red) and dextral (antithetic, blue) relative movement,  
 412 respectively. The last panel for each series shows a surface photograph of the final stage overlain with the  
 413 interpreted fault pattern; red lines are sinistral faults, blue lines are dextral faults, green line indicates reverse  
 414 fault.

415

416

417

418

419 **5.4. Discussion**

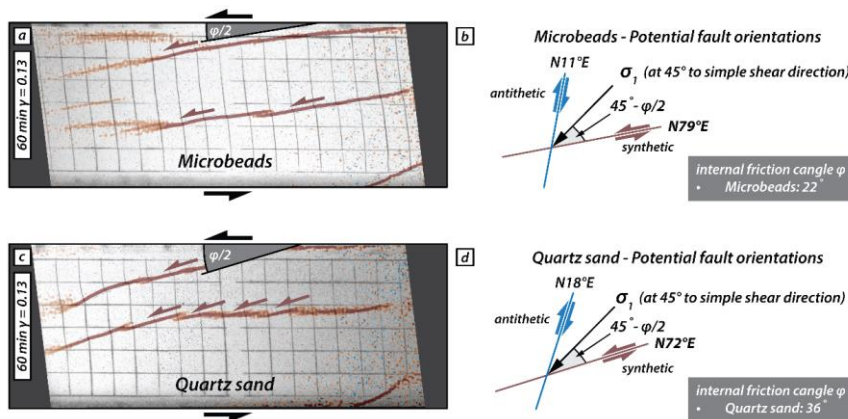
420 ~~We performed analogue modelling experiments to test the influence of vertical, upper crustal domains of~~  
421 ~~contrasting strength on the development and evolution of strike-slip fault zones. We first discuss the fault~~  
422 ~~kinematics of two reference models which simulated a uniform upper, brittle crust (section 4.1).~~  
423 ~~Subsequently, we discuss and compare the results of three series of models (Series B, C and D, in which~~  
424 ~~two different brittle materials, strong quartz sand and weak microbeads, alternated to form three vertical~~  
425 ~~domains of contrasting strength (section 4.2), i.e. either weak-strong-weak (i.e. quartz sand-microbeads-~~  
426 ~~quartz sand) or strong-weak-strong (i.e. microbeads-quartz sand-microbead section). Each of these three~~  
427 ~~series had a different orientation of the vertical domains with respect to the shear direction. In section 4.3~~  
428 ~~we discuss how the central vertical domain affects fault interaction and/or fault linkage. In the final section~~  
429 ~~4.4 we compare modelling results with a strike-slip fault system in the Iberian Peninsula.~~

430 **5.2.4.1. Series A: Strike-slip faulting in models with a homogeneous upper brittle layer crust**  
431 **model**

432 ~~In our models simulating homogeneous crust the structures display an *en echelon* pattern, as should be~~  
433 ~~expected (Bartlett et al., 1981; Sylvester, 1988; Misra et al., 2009). Initial bulk simple shear is~~  
434 ~~accommodated in both models by zones of diffuse deformation and is followed by localized deformation~~  
435 ~~along narrow fault zones. It is interesting to note that localization requires a higher shear deformation in~~  
436 ~~the model with the weak microbeads-material than in the model with quartz sand with strong material. This~~  
437 ~~difference in localization behaviour is attributed to the difference in dilatancy between the two analogue~~  
438 ~~materials, which is closely related to grain shape and grain size distribution. The weak material, represented~~  
439 ~~by the microbeads, are well-rounded and have a narrow grain size distribution (150-210 µm), whereas the~~  
440 ~~strong material (quartz sand grains) areis angular and have a wider grain size distribution (60-250 µm). The~~  
441 ~~more equal-uniform the grain shape and grain size, the more applied shear deformation is needed before~~  
442 ~~strain localizesto localize the strain along a narrow fault zone (Antonellini et al., 1995; Mair et al., 2002).~~  
443 ~~Therefore, the shape and grain-size characteristics will influence the time that a fault may take to reactivate~~  
444 ~~depending on the lithology that comprises its fault zone (e.g. Sammis et al., 1987; Mair et al., 2002).~~

Con formato: Fuente: Cursiva

445 ~~In these two models~~ sinistral (synthetic) strike-slip faults form ~~first in both models~~. The initial strike of  
446 these faults differs between the model with ~~microbeads the weaker material~~ and the one with ~~quartz~~  
447 ~~sand strong material~~, striking at ~~e-~~N79°E and N72°E, respectively. ~~The internal friction angle of each type~~  
448 ~~of material will be adjusted to a certain orientation of rupture according to the Mohr-Coulomb criterion.~~  
449 ~~The synthetic fault orientations reflect the Mohr-Coulomb fracture criterion for faulting in a homogeneous~~  
450 ~~material~~ (Fig. 7). At the ~~onset of simple shear beginning of the experiment~~, the main principal stress ( $-\sigma_1$ )  
451 is oriented at 45° to the shear direction, and the two potential fault orientations strike at  $45^\circ - \phi/2$  and at  
452  $45^\circ + \phi/2$  to  $\sigma_1$ , respectively with  $\phi$  the angle of internal peak friction, ~~which is 22° for the microbeads~~  
453 ~~and 36° for quartz sand (Fig. 7). Hence i.e.,~~ the synthetic and antithetic faults ~~would~~ strike at N79°E and  
454 N11°E, respectively in the model with microbeads and at N72°E and N18°E, ~~respectively~~ in the model  
455 with quartz sand ~~respectively~~. ~~In our models only the synthetic faults form during the early stages of simple~~  
456 ~~shear deformation. The early synthetic faults form a right-stepping en echelon fault pattern that link up with~~  
457 ~~increasing deformation to form major strike slip faults.~~ The fact that nearly all deformation is ~~taken~~  
458 ~~up~~ accommodated by synthetic faults is typical of simple shear models with an initial rectangular shape, i.e.  
459 a large aspect ratio of length (parallel to shear direction) divided by width (Schreurs, 2003; Dooley &  
460 Schreurs, 2012). A comparison of previous simple shear experiments shows that the shape of the initial  
461 model has ~~an clear~~ influence on the relative proportion of synthetic and antithetic faults (Gapais et al., 1991;  
462 Schreurs, 2003). With decreasing aspect ratio, the number of antithetic faults will increase, and in case of  
463 an initially square-shaped model, (i.e., aspect ratio is 1) antithetic faults will dominate (Gapais et al., 1991;  
464 Dooley & Schreurs, 2012). In the model with quartz sand, a few antithetic faults form in between previously  
465 formed major synthetic faults (Fig. 3i). These late antithetic faults, however, form in response to local stress  
466 field modifications between overlapping synthetic faults, causing  $\sigma_1$  to rotate clockwise from 45° to the  
467 bulk shear direction towards an orientation that is subparallel to the previously formed synthetic faults. As  
468 a consequence, these late antithetic faults are not in the “conjugate” position with respect to the synthetic  
469 major faults, but strike at lower angles with respect to the long borders of the model (these are the lower-  
470 angle antithetic faults of Schreurs, 2003).



Con formato: Espacio Después: 0 pto, Interlineado: Múltiple 1,15 lin.

471

472 **Figure 7:** Illustrative scheme of the expected fault orientation according to the Mohr-Coulomb failure criteria, for the experiments with only one type of material (homogeneous upper crust). a) and c) Surface photographs of the model with microbeads only (a) and quartz sand only (c), with the incremental vorticity after 60 minutes (40 mm displacement). b) and d) Schematic explanation for the expected orientation of the synthetic and antithetic faults considering the simple shear orientation along with the Mohr-Coulomb failure criteria, for the models with microbeads and quartz sand only respectively.

478

Con formato: Espacio Después: 0 pto

479 **5.3.4.2. Series B, C and D: The influence of the orientation of vertical domains of contrasting lateral heterogeneities on brittle strength on strike-slip faulting**

480

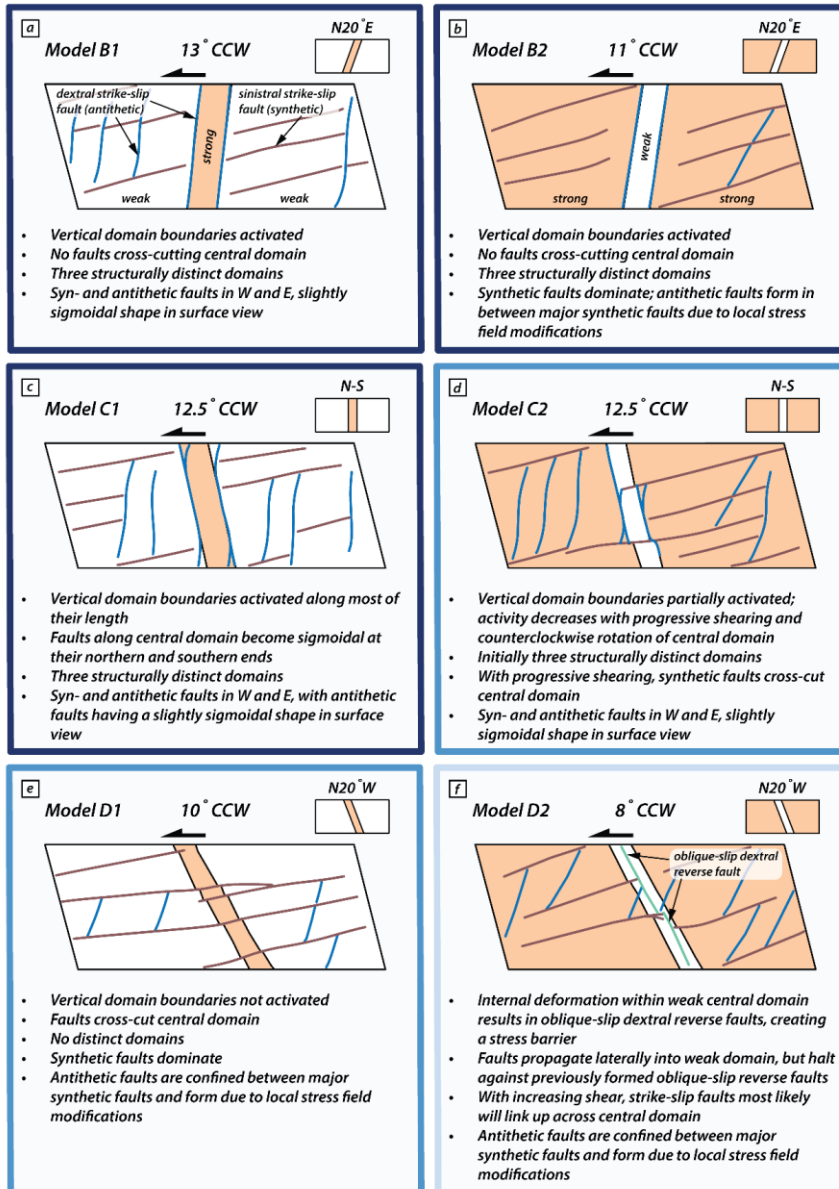
481 Introducing a vertical domain of contrasting brittle strength in our with different properties that the surrounding material results in different fault patterns and timing of the structures (Segall and Pollard, 1983; Peacock, 1991; Peacock and Sanderson, 1992; Schellart and Strak, 2016; Lefevre et al., 2020; Livio et al., 2019; Venancio and Alves Da Silva, 2023). The degree of difference in the fault pattern is a function of the orientation and the strength of the domains.

Con formato: Fuente: 10 pto

486 models results in fault patterns that differ when compared to the Series A models that consisted only of one homogeneous brittle material. The degree of difference in the fault pattern is a function of the orientation of the vertical domains and whether the domains have a strong (quartz sand) or weak (microbeads) material in the central domain. Fig. 8 shows a schematic overview of the final structures of all six models which had vertical domains of contrasting brittle strength. Each of these six models had an initial rectangular shape and consisted of a western, central and eastern domain with the central one having a contrasting brittle strength with respect to the adjacent, outer domains. The initial strike of the vertical domain boundaries, either  $N20^\circ E$ , N-S or  $N20^\circ W$  has a profound influence on the resulting fault pattern.

493





494

495 Figure 8: Schematic surface views summarizing the main results from the models with vertical domains of  
 496 contrasting brittle strength.

497

498 ~~The first thing noticed is that the faults do not follow the *en echelon* pattern and the antithetic faults are the~~  
499 ~~first one to be form (Figs. 4 and 5). The domain boundaries in Series B and C models initially strike N20°E~~  
500 ~~and N-S respectively (Fig. 8a, b, c and d), which is close to the antithetic fault orientation predicted by the~~  
501 ~~Mohr-Coulomb failure criterion (i.e. N11°E for microbeads and N18°E for quartz sand, see section 4.1).~~  
502 ~~(i.e. N11°E for microbeads and N18°E for quartz sand, see section 4.1). As a result~~~~result~~, the domain  
503 boundaries in both models are activated along their entire length, ~~and forming antithetic, dextral~~~~the~~  
504 ~~antithetic faults are formed~~ ~~strike-slip faults~~ along the borders of the central domains ~~them~~ (Fig. 8a, b and  
505 ~~c,d~~). With progressive sinistral simple shear, the central domain bounded by the fault rotates ~~the central~~  
506 ~~fault bounded domain rotates~~ counterclockwise about a vertical axis, and at the end of the experiment has  
507 rotated ~~ed by~~ about 12° striking ~~e-~~N08°E. The faults of the domain boundaries remain active throughout the  
508 model run, because their strike ~~is favorably oriented respect the main stress (Fig 8a, b).~~ ~~orientation remains~~  
509 ~~close to the antithetic fault orientation predicted by the Mohr-Coulomb failure criterion (Fig 8a, b).~~ As a  
510 result of continuous fault activity along the central domain boundaries, ~~the sinistral faults in the series B~~  
511 ~~and in model C1 cannot propagate along the entire model, regardless of the composition of the central~~  
512 ~~domain, and two possibilities are shown: the faults are segmented (Fig 8a and b) or more new faults are~~  
513 ~~generated in the eastern and western domains (Fig. 8c). However, if the central domain is composed of the~~  
514 ~~weak material and is not fully surrounded by antithetical faults, the synthetic fault can crosscut the entire~~  
515 ~~model (Fig. 8d). This may offer the possibility that strike-slip fault stepping may also be due to the action~~  
516 ~~of lithology, which is able to induce fault segmentation. Hence, the presence laterally heterogeneous upper~~  
517 ~~crust with steep boundaries and suitable oriented for activation by antithetic faults, can prevent the synthetic~~  
518 ~~strike-slip faults from crossing certain domains.~~

Con formato: Fuente: Cursiva

Con formato: Sin Resaltar

Con formato: Sin Resaltar

Con formato: Sin Resaltar

519 ~~The antithetic faults that form in the outer domains of our models are of two types: (i) those that form~~  
520 ~~relatively early in as yet largely unfaulted domains and strike at large angles to the shear direction (Fig. 8a,~~  
521 ~~c and d) and (ii) those confined between earlier formed and overlapping synthetic faults that strike at lower~~  
522 ~~angles to the shear direction (Fig. 8b, e and f). In the first case, the early-formed antithetic faults reflect the~~  
523 ~~orientation predicted by the Mohr-Coulomb failure criterion: striking N18°E if the outer domains consist~~  
524 ~~of the strong material and N11°E if the outer domains consist of the weak material. Due to lateral fault~~  
525 ~~propagation and coeval rotation of the central fault segments, these antithetic faults obtain a slightly~~  
526 ~~sigmoidal shape form in map view during progressive simple shear (see also Schreurs, 1994, 2003; Dooley~~  
527 ~~and Schreurs, 2012). In th second case, the antithetic faults confined in between closely spaced, earlier~~

528 formed, synthetic faults have an initial different strike (N15°-N20°E in the weak material, e.g. Model C1)  
529 and N25°- N30°E in the strong material, (e.g. Model C2). The antithetic faults confined between major  
530 synthetic faults result from local stress field modifications governed by relative movement of material in  
531 between previously formed synthetic faults with large overlap (Schreurs, 2003; Dooley and Schreurs, 2012;  
532 their R<sub>1</sub> faults). Both types of antithetic faults rotate counterclockwise with progressive sinistral simple  
533 shear. Rotation of faults and blocks in strike-slip fault systems is not only observed in analogue models  
534 (Schreurs, 1994, 2003; Dooley and Schreurs, 2012), but has also been documented in nature (e.g., Ron et  
535 al., 1986; Nicholson et al., 1986). It is thus important to keep in mind that antithetic faults (and blocks in  
536 between) can undergo considerable rotation about a vertical axis during simple shear deformation, implying  
537 that present-day antithetic fault orientations in strike-slip fault systems do not necessarily reflect the  
538 orientations in which they initially formed.

539 ~~each of the two Series D models develops three spatially-separated structural domains: a western and eastern~~  
540 ~~domain, containing both synthetic and antithetic faults, separated from a central domain bordered by~~  
541 ~~antithetic faults. Faulting is thus compartmentalized within the model and no faults propagate from the~~  
542 ~~outer domains into the central domain (Fig. 8a, b).~~

543 ~~In comparison to the Series B models, the initial N-S strike of the central domain boundaries in the Series~~  
544 ~~C models (Fig 8c, d) is less favorably oriented with respect to the antithetic fault orientations predicted by~~  
545 ~~the Mohr-Coulomb failure criterion. As a result, the domain boundaries in both models are only partially~~  
546 ~~activated dextrally during initial simple shear deformation (Fig. 4). During progressive shearing the domain~~  
547 ~~boundaries rotate counterclockwise and become even less favorably oriented for further activation and fault~~  
548 ~~branches partially no longer follow the domain boundaries, with the overall fault geometry at and in the~~  
549 ~~vicinity of the central domain boundaries acquiring an overall “S-shaped” geometry in surface view (Fig.~~  
550 ~~8c, d). The difference between Model C1 (weak-strong-weak) and Model C2 (strong-weak-strong) is that~~  
551 ~~in the former the total length of the domain boundaries activated is larger and faults at or in the immediate~~  
552 ~~vicinity of the domain boundaries remain longer active than in the latter (compare Fig. 8c and d). This~~  
553 ~~difference can be explained by the fact that in Model C1 the weak microbeads represent the dominant brittle~~  
554 ~~material, and the antithetic fault orientation predicted by Mohr-Coulomb, N10°E for a homogeneous~~  
555 ~~microbeads layer, is close to the initial N-S orientation of the domain boundary. In contrast, Model C2 is~~  
556 ~~dominated by quartz sand and the antithetic fault orientation predicted by Mohr-Coulomb, N18°E for a~~

Comentado [SG1]: From this line to the end of the section  
I'm not sure what is the best way to shortening it

557 homogeneous quartz sand layer, is farther away from the initial N-S striking central domain and  
558 consequently domain boundaries are less activated and fault activity decreases more rapidly with  
559 progressive deformation. As a consequence in Model C2, synthetic faults forming in the outer domains can  
560 propagate across the poorly activated domain boundaries, cross-cutting the central domain, and can partly  
561 link up to form major through-going faults. In Model C1, however, fault activity along domain boundaries  
562 was stronger and occurred longer, and the domain boundaries form a more effective barrier and no synthetic  
563 faults cross-cut the central domain.

564 In comparison with the Series B and Series C models, the initial N20°W striking central domain boundaries  
565 in the Series D models are the least favorably oriented for antithetical fault activation. Consequently, the  
566 fault development pattern follows an echelon type, but in both cases the size of the segments is affected by  
567 the lateral variation of the material properties. In the weak-strong-weak Model D1 (Fig. 8-e and f), the  
568 domain boundaries are not activated at all and the synthetic faults forming in the outer domains propagate  
569 across the central domain. Apart from a slight re-orientation of the fault strike, reflecting the difference in  
570 material strength between central and outer domains (difference in internal friction angles), the fault pattern  
571 in Model D1 is ~~very~~ similar to the one in Model A1, which had no vertical brittle strength contrasts. The  
572 strong-weak-strong Model D2 shows a different deformation behaviour. Although the domain boundaries  
573 at the surface are not activated, the presence of a weak material surrounded by strong material results in  
574 internal deformation within the central domain and dextral oblique-slip reverse faults form striking parallel  
575 to the domain boundaries. These faults prevent synthetic faults from crossing the central domain, and they  
576 halt against the oblique-slip reverse faults.

577 In all models with vertical domains of contrasting brittle strength, the orientation of the sinistral, synthetic  
578 faults forming in the outer domains reflects the Mohr-Coulomb failure criterion, i.e. if the outer domains  
579 consist of weak microbeads, with an internal friction angle of 22°, the strike of the synthetic faults is e.  
580 N79°E and when the outer domains consist of strong quartz sand, with an internal friction angle of 36°, the  
581 strike of the synthetic faults is e. N72°E (see also section 4.1). In those models, in which the synthetic faults  
582 cross-cut the central domain, the strike of the faults changes slightly, due to the difference in internal friction  
583 angles between the quartz sand and the microbeads (Du and Aydin, 1995; de Doney et al., 2011).

584 ~~The antithetical faults that form in the outer domains of our models are of two types: (i) those that form~~  
585 ~~relatively early in as yet largely unfaulted domains and strike at large angles to the shear direction and (ii)~~

Con formato: Resaltar

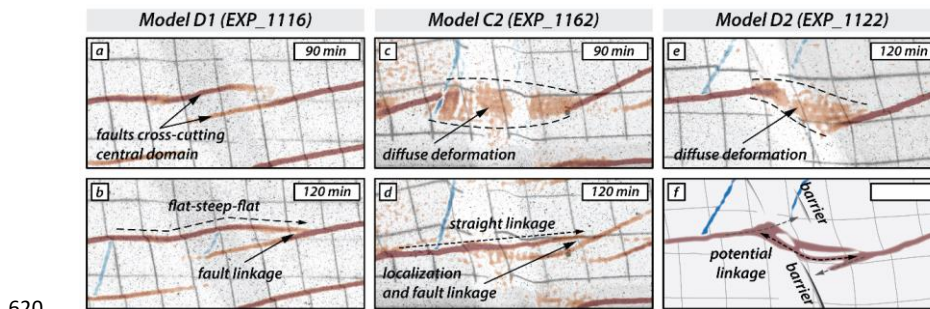
586 those confined between earlier formed and overlapping synthetic faults that strike at lower angles to the  
587 shear direction. The early formed dextral, antithetic faults reflect the orientation predicted by the Mohr-  
588 Coulomb failure criterion, striking c. N18°E if the outer domains consist of quartz sand and c. N11°E if the  
589 outer domains consist of microbeads. Due to lateral fault propagation and coeval rotation of the central fault  
590 segments, these antithetic faults obtain a slightly S-shaped sigmoidal form in map view during progressive  
591 simple shear (see also Schreurs, 1994, 2003; Dooley and Schreurs, 2012). The antithetic faults that are  
592 confined in between closely spaced, earlier formed, synthetic faults have an initial different strike (c. N15°-  
593 N20°E in microbeads domains, e.g. Model C1) and c. N25°-N30°E in quartz sand domains, (e.g. Model  
594 C2), which is clearly different from those antithetic faults formed during early stages in largely unfaulted  
595 domains. The antithetic faults confined between major synthetic faults result from local stress field  
596 modifications governed by relative movement of material in between previously formed synthetic faults  
597 with large overlap (Schreurs, 2003; Dooley and Schreurs, 2012; their R<sub>L</sub> faults). Both types of antithetic  
598 faults rotate counterclockwise with progressive sinistral simple shear. Rotation of faults and blocks in  
599 strike-slip fault systems is not only observed in analogue models (Schreurs, 1994, 2003; Dooley and  
600 Schreurs, 2012), but has also been documented in nature (e.g., Ron et al., 1986; Nicholson et al., 1986). It  
601 is thus important to keep in mind that antithetic faults (and blocks in between) can undergo considerable  
602 rotation about a vertical axis during simple shear deformation, implying that present day antithetic fault  
603 orientations in strike-slip fault systems do not necessarily reflect the orientations in which they initially  
604 formed.

#### 606 **5.4.4.3. Fault linkage across central domain**

607 In models where synthetic faults from the eastern and western domain cross-cut the central domain, the  
608 entire model behaves as one domain. As shown in the section above, this is the case for models C2, D1,  
609 and D2 where the vertical boundaries of the central domain are not or only partially activated, depending  
610 on the orientation of the central domain (section 4.2). However, all three models show distinct differences  
611 in how laterally propagating synthetic strike-slip faults link across the central domain (Fig. 9). For model  
612 D1 (Fig. 9a, b), faults cross-cut the stronger (i.e., quartz sand) central domain from the eastern-E and  
613 Wwestern domains (Fig. 9a) and eventually link in the E domain linking up in a new segment. This new  
614 segment shows different orientation resulting in a step-like linkage pattern in surface view (i.e., flat-steep-

615 flat; Fig. 9a, b). (Fig. 9b). When segmentation occurs and the faults cross the central domain, the orientation  
 616 of the faults is different, probably related to the internal friction angles between the quartz sand and the  
 617 microbeads (Du and Aydin, 1995; de Doney et al., 2011).

618 Across the central domain, the fault strike changes according to the predicted Mohr-Coulomb failure  
 619 criterion resulting in a step-like linkage pattern in surface view (i.e., flat-steep-flat; Fig. 9a, b).



620

621 **Figure 9:** Surface detailed photographs of the central domain of the models with the contrasting brittle  
 622 mechanical strength, showing the fault linkage across the central domain at 90 minutes (60 mm displacement)  
 623 and 120 minutes (80 mm displacement). a) and b) model D1 with the central domain striking N20°W and  
 624 composed by the strong material (quartz). c) and d) model C2 with the central domain striking N-S and  
 625 composed by the weak material (microbeads). e) model D2 with the central domain striking N20°W and  
 626 composed by the weak material (microbeads). f) Schematic drawing for the fault linkage at the last stage.

627

628 For models C2 and D2, however, the domain configuration strong-weak-strong has implications for fault  
 629 linkage. As synthetic strike-slip faults propagate from the western and eastern domains towards the weaker  
 630 central domain, early deformation patterns are characterized by a zone of diffuse deformation across the  
 631 central domain (Fig. 9c, e). In model C2, the fault from the W domain cross-cuts the weak central domain  
 632 and eventually links with the fault in the E domain in a straight fashion after 120 min (Fig. 9d), abandoning  
 633 earlier active fault strands striking N18°E (i.e., the predicted orientation for Mohr-Coulomb failure  
 634 criterion). Similar fault kinematics should be expected for model D2 (Fig. 9e, f). However, laterally  
 635 propagating faults in the western and eastern domain do not link during the duration of the model run.  
 636 Instead, the two fault segments halt at the domain boundary resulting in ongoing diffuse deformation  
 637 without strain localization in the central domain. This behavior may be explained by the presence of the  
 638 N20°W-striking reverse faults within the central model domain. Due to the misalignment between central  
 639 domain boundaries and the expected orientation of antithetic faults, the domain boundaries do not activate

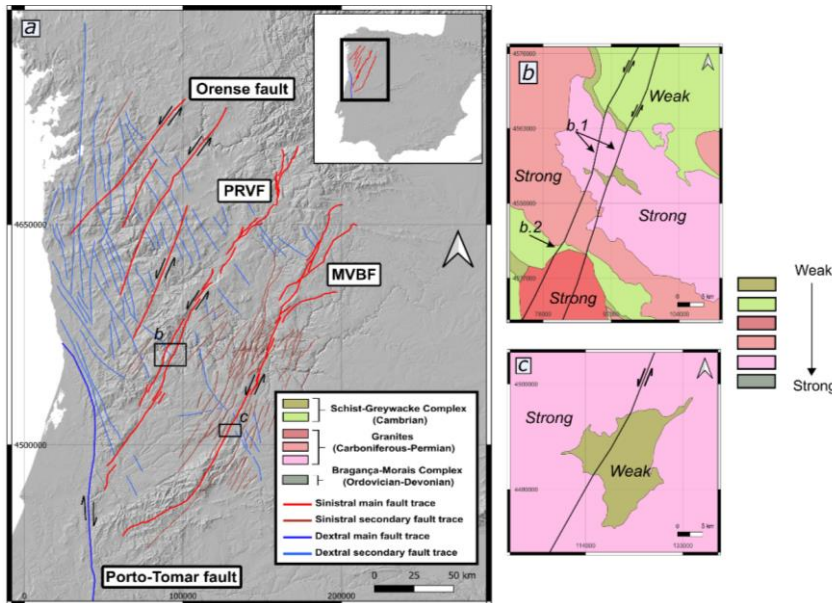
640 and domain-internal deformation is taken up by oblique-slip dextral reverse faults. Such faults (i.e., nearly  
641 orthogonally striking with respect to synthetic faults) accommodate bulk shear deformation hindering the  
642 synthetic faults to propagate. In that sense, the oblique-slip reverse faults act as an impenetrable barrier  
643 inhibiting linkage of synthetic faults across the weak central domain (Fig. 9f). Oblique-slip reverse faults  
644 in the central domain, therefore, influence fault interaction across the central domain in a similar way as do  
645 the activated domain boundaries in models B1, B2, and C1 (Fig. 8).

646

647

#### 648 **5.5.4.4. Comparison with strike-slip fault zones in Iberia**

649 The NW Iberian Peninsula contains major sinistral and dextral strike-slip intraplate fault systems (Fig. 10a).  
650 These ~~groups on~~ intraplate fault systems are located in an old basement developed during Variscan Orogeny  
651 (Devonian-Carboniferous, e.g., Matte, 1991; Martínez Catalán et al., 1997; Fernández et al., 2004), during  
652 this stage a set of lithologic units with contrasting properties such as granites, quartzites, slates and high-  
653 grade metamorphic rocks were emplaced and deformed. During the Alpine Compression (Late Cretaceous  
654 to the present), the present fault pattern was obtained due to the collision between the Iberian microplate  
655 and the northern edge of Africa in the middle Miocene (e. g., Alonso et al., 1996; Vegas et al., 2004; Martín-  
656 González and Heredia, 2011, Martín-González et al., 2012). This collision caused the Iberian Peninsula to  
657 undergo a counterclockwise twist, resulting in slight shearing (e.g. Martínez Catalán, 2011; Vergés et al.,  
658 2019). In the study area, intraplate deformation led to a fault pattern primarily composed of sinistral faults,  
659 such as the Penacova-Régua-Verin (PRVF), Manteigas-Vilariça-Bragança (MVBF), and Orense faults (see  
660 Fig. 10a). Additionally, antithetic dextral faults were also generated (see Fig. 10a).



661

662 **Figure 10:** a) Digital elevation model of the northwest section of the Iberian Peninsula where the main faults  
663 are drawn, with the location of Figures b and c. The faults are essentially sinistral and there is a dextral fault on  
664 the southern edge that delimits the study area. In blue and light red, the secondary antithetic (dextral) and  
665 synthetic (sinistral) faults have been marked respectively. b) Schematic representation of the southern section  
666 of the Verin fault showing patterns of directional changes similar to models D1 and D2. c) Schematic  
667 representation of the southern section of the Vilarica fault showing a similar deformation pattern to model C2.

668

669 Among the traces of these faults, we can observe antithetic faults that do not connect with each other and,  
670 in some cases, acquire a sigmoidal S-shape as described-observed in Modelsthe C1 and C2 models (Fig.  
671 8e and f). These antithetic faults are not in a conjugate position and are-mostly confined between-the  
672 major sinistral faults. At the end of the sinistral faults is the Porto-Tomar fault, which delimits the study  
673 area. The Porto-Tomar fault shows dextral displacement and tectonically delimits the area to the north and  
674 south of Portugal (Veludo et al., 2017). The main traces of the sinistral faults is-are not completely straight  
675 straight, but show slight changes in strike. For example, along the PRVF, the fault undergoes a  
676 counterclockwise refraction when crossing from weak into strong lithologies (b.1 in Fig. 10b), similar to  
677 Model D1 with strong quartz sand in the central domain (Fig. 10b). On the other hand, the same fault  
678 undergoes a clockwise refraction as it crosses from strong lithologies (granites) in shaly units (b.2 in Fig.  
679 10b), similar to Model D2 with weak microbeads in the central domain. The same phenomenon is also  
680 observed along the Vilarica fault when the fault intersects granites and slate units (Fig. 10c), and-undergoes



681 small changes that are observable at a larger scale (Fig. 10b and c). Along the same trace of the PRV fault,  
682 it is observed that the faults undergo a counterclockwise refraction, similar to the D1 model with quartz in  
683 the central domain (Fig. 10b). On the other hand, in section b.2, the fault undergoes a clockwise refraction  
684 as it crosses shale-type materials (which is represented by the microbeads grains in our models; Panien et  
685 al., 2006), similar to the D2 experiment. This phenomenon is also observed in the Vilarica fault when the  
686 fault intersects granites and slates units (Fig. 10c).

687 Although on a local scale, similarities are observed in the behaviour of individual faults crossing contrasting  
688 lithologies in nature and faults crossing vertical domain boundaries in our analogue models, the NW Iberian  
689 Peninsula strike-slip fault system as a whole does show little resemblance with the overall fault patterns in  
690 homogeneous or laterally heterogeneous upper crustal models. This may indicate that the NW Iberian crust  
691 is much more heterogeneous and complex than the one modelled in our experiments.

692

693

## 694 **6.5. Conclusions**

695 We performed a series of analogue models to investigate faulting in the upper, brittle crust as a result of  
696 sinistral simple shear. ~~The initial model had a rectangular shape with the long axis parallel to the shear~~  
697 ~~direction.~~ In a first series of models, the upper crust was homogeneous and consisted of a single analogue  
698 material, either weak microbeads or strong quartz sand. In two reference models, the brittle crust consisted  
699 of either a weak granular material (microbeads) or a strong granular material (quartz sand). In three further  
700 series of models, the upper crust is laterally heterogeneous and consisted of three domains with vertical  
701 boundaries and contrasting strength (i.e. a weak-strong-weak or a strong-weak-strong configuration). ~~In a~~  
702 ~~further six models, we introduced mechanical strength contrasts in the upper crust, by introducing a vertical~~  
703 ~~central domain consisting of quartz sand surrounded by microbeads (i.e. a weak-strong-weak configuration)~~  
704 ~~or the other way around (i.e. a strong-weak-strong configuration).~~ These models allowed us to test the  
705 influence of vertical domains of contrasting brittle strength on the fault pattern, and the influence of the  
706 weak-strong-weak and strong-weak-strong configuration.

707 —The fault pattern of models with a single granular material simulating the upper crust (i.e. no vertical  
708 domains of contrasting brittle mechanical strength) in a homogeneous upper crust is dominated by  
709 sinistral (synthetic) strike-slip faulting, whose orientations are readily explained by the Mohr-Coulomb  
710 failure criterion, with fault strikes being a function of the internal friction angles, which differ between  
711 microbeads ( $\phi=22^\circ$ ) and quartz sand ( $\phi=36^\circ$ )

712 - In models with vertical domains of contrasting brittle strength heterogeneous upper crust, the  
713 development of the faults does not follow an *en echelon* pattern. The sinistral faults are developed  
714 initial fault development occurs in the outer domains, with syn and antithetic faults forming in the  
715 expected orientations according to the Mohr-Coulomb failure criterion.

716 —The heterogeneity of the upper crust, as lateral variations of the lithology, could affect the expected  
717 sequence of strike-slip faults with antithetic faults being the first to form. If the initial strike of the  
718 boundaries of the domains is subparallel to the predicted Mohr-Coulomb, the development of antithetic  
719 faults is promoted. As a consequence, faulting may occur in distinct structural domains and faults may  
720 be segmented. In models with domains of contrasting brittle strength, the central domain boundaries are almost  
721 completely or fully activated if their strike orientation is subparallel to the predicted antithetic fault orientation.  
722 As a consequence, faulting occurs in three distinct structural domains.

723 - If the orientation of the domain boundaries is less favorably favorable, the development of antithetic  
724 faults is not promoted, oriented, they are only partially activated or not at all, allowing synthetic faults  
725 that to form without in the outer domains to cut across the central domain. Hence, there are no distinct  
726 structural domains.

727 - The properties of the lithology that intersect the sinistral faults, influences how their segments are  
728 connected. If the central domain boundaries are fully activated and three structurally distinct domains  
729 form, the strength contrast between the domains (i.e. weak-strong-weak or strong-weak-strong) does  
730 not influence the overall fault pattern. However, if the domain boundaries remain inactive then the  
731 strength contrast between the domains has an influence on the fault development and evolution. In the  
732 case of weak-strong-weak, the synthetic faults from the outer domains cross-cut the central domain  
733 with a slight change in strike orientation, whereas in the case of strong-weak-strong, the weak central  
734 domain show internal oblique-slip reverse faulting, which inhibits faults from the outer domain to fully  
735 cross the central domain.

736 —Although we only tested sinistral simple shear, our results can also be applied to dextral simple shear  
737 by mirroring the fault patterns around a N-S axis.

Con formato: Fuente: Cursiva

Con formato: Fuente: (Predeterminada) Times New Roman, 10 pto

Con formato: Inglés (Estados Unidos)

Con formato: Inglés (Estados Unidos)

738 -

739 ~~There are similarities between the behaviour of individual faults in natural systems and our~~  
740 ~~heterogeneous upper crustal models, i.e. the slight change in strike orientation when crossing a~~  
741 ~~boundary with contrasting strength. Our results are comparable with the fault systems observed in the~~  
742 ~~NW of the Iberian Peninsula. The area shows synthetic and antithetic faults whose distribution is~~  
743 ~~similar to the models made. In addition, refraction patterns of the main trace of the faults associated~~  
744 ~~with lithological contrasts can be observed.~~

745 -

746

#### 747 **7.6. Competing interests**

748 The contact author has declared that none of the authors has any competing interests.

#### 749 **8.7. Acknowledgments**

750 The following work has been partially funded by a predoctoral contract (PREDOC20-073), by the  
751 Universidad Rey Juan Carlos and project PID2022-139527OB-I00 funded by  
752 MCIN/AEI/10.13039/501100011033/ and FEDER.

753

#### 754 **9.8. References**

- 755 [Alonso, J. L., Pulgar, J. A., García-Ramos, J. C., & Barba, P.: Tertiary basins and Alpine tectonics in the](#)  
756 [Cantabrian Mountains \(NW Spain\). in Tertiary Basins of Spain \(pp. 214–227\). Cambridge](#)  
757 [University Press, 1996](#)
- 758 Aki, K.: Geometric features of a fault zone related to the nucleation and termination of an earthquake  
759 rupture, in: Proceedings of Conference XLV Fault Segmentation and Controls of Rupture Initiation  
760 and Termination. US Geological Survey Open File Report 89-315, pp. 1–9, 1989
- 761 ~~Arthaud, F., Matte, Ph.: Les décrochements tardi hercyniens du sud ouest de l'europe. Geometrie et essai~~  
762 ~~de reconstitution des conditions de la deformation. Tectonophysics 25, 139–171.~~  
763 ~~[https://doi.org/10.1016/0040-1951\(75\)90014-1](https://doi.org/10.1016/0040-1951(75)90014-1), 1975.~~
- 764 Anderson, E. M.: The Dynamics of faulting and Dyke Formation with Applications to Britain (2nd edition),  
765 Oliver and Boyd, Edinburgh, Scotland, 1951.
- 766 Antonellini, M.A., Aydin, A., Pollard, D.D.: Microstructure of deformation bands in porous sandstones at  
767 Arches National Park, Utah. [Journal of Structural Geology](#) *J. Struct. Geol.*, 16, 941e959, 1994.
- 768 Aydin, A., Nur, A.: Evolution of pull-apart basins and their scale independence. *Tectonics* 1, 91–105, 1982.
- 769 Aydin, A.: Fractures, faults, and hydrocarbon entrapment, migration and flow. [Marine and Petroleum](#)  
770 [Geology-Mar. Pet. Geol.](#), 17, 797–814, 2000.

Con formato: Fuente: (Predeterminada) Times New Roman, 10 pto

Con formato: Párrafo de lista, Con viñetas + Nivel: 1 + Alineación: 0 cm + Sangría: 0,63 cm

Con formato: Inglés (Estados Unidos)

Con formato: Espacio Después: 0 pto

<p>771 Aydin, A., &amp; Berryman, J. G: Analysis of the growth of strike-slip faults using effective medium theory. <i>J.</i>  772 <i>Struct. Geol., Journal of Structural Geology</i>, 32(11), 1629–1642.  773 <a href="https://doi.org/10.1016/j.jsg.2009.11.007">https://doi.org/10.1016/j.jsg.2009.11.007</a>, 2010.</p> <p>774 Barka, A., Kadinsky-Cade, K.: Strike-slip fault geometry in Turkey and its influence on earthquake activity.  775 <i>Tectonics</i>, 7, 663–684, 1988.</p> <p>776 <a href="https://doi.org/10.1016/0040-1951(81)90116-5">Bartlett, W.L., Friedman, M., Logan, J.M: Experimental folding and faulting of rocks under confining  777 pressure Part IX. Wrench faults in limestone layers. <i>Tectonophysics</i>, 79, 255–277.  778 <a href="https://doi.org/10.1016/0040-1951(81)90116-5">https://doi.org/10.1016/0040-1951(81)90116-5</a>, 1988.</a></p> <p>779</p> <p>780 <a href="https://doi.org/10.1016/j.jsg.2013.10.008">Bullock, R. J., De Paola, N., Holdsworth, R. E., &amp; Trabucho-Alexandre, J.: Lithological controls on the  781 deformation mechanisms operating within carbonate-hosted faults during the seismic cycle. <i>J.</i>  782 <i>Struct. Geol.</i>, 58, 22–42. <a href="https://doi.org/10.1016/j.jsg.2013.10.008">https://doi.org/10.1016/j.jsg.2013.10.008</a>, 2014.</a></p> <p>783 <a href="https://doi.org/10.1113/1139">Boutelier, D., Schrank, C., Regenauer Lieb, K.: 2-D finite displacements and strain from particle  784 imaging velocimetry (PIV) analysis of tectonic analogue models with TecPIV. <i>Solid Earth</i>  785 10, 1123–1139, 2019.</a></p> <p>786 Burgmann, R., Pollard, D.D.: Strain accommodation about strike-slip fault discontinuities in granitic rock  787 under brittle-to-ductile conditions. <i>J. Struct. Geol., Journal of Structural Geology</i>–16, 1655–1674,  788 1994.</p> <p>789 <a href="https://doi.org/10.1016/j.precamres.2021.106365">Byerlee, J.: Friction of rocks, pages 615–626. Springer, 1978.</a></p> <p>790</p> <p>791 <a href="https://doi.org/10.1007/s00024-009-0511-4">Cazarin, C.L., van der Velde, R., Santos, R.V., Reijmer, J.J.G., Bezerra, F.H.R., Bertotti, G., La Bruna, V.,  792 Silva, D.C.C., de Castro, D.L., Srivastava, N.K., Barbosa, P. F.: Hydrothermal activity along a  793 strike-slip fault zone and host units in the S’ ao Francisco Craton, Brazil – implications for fluid  794 flow in sedimentary basins. <i>Precambrian Res.</i> 365  795 <a href="https://doi.org/10.1016/j.precamres.2021.106365">https://doi.org/10.1016/j.precamres.2021.106365</a>, 2021.</a></p> <p>796</p> <p>797 Cheng, X., Ding, W., Pan, L., Zou, Y., Li, Y., Yin, Y., &amp; Ding, S.: Geometry and kinematics characteristics  798 of strike-slip fault zone in complex structure area: A case study from the south no. 15 strike-slip  799 fault zone in the Eastern Sichuan Basin, China. <i>Frontiers in earth scienceFront. Earth Sci.</i>, 10.  800 <a href="https://doi.org/10.3389/feart.2022.922664">https://doi.org/10.3389/feart.2022.922664</a>, 2022.</p> <p>801 <a href="https://doi.org/10.1130/GES02179.1">Cooke, M. L., Toeneboehn, K., and Hatch, J. L.: Onset of slip partitioning under oblique  802 convergence within scaled physical experiments, <i>Geosphere</i>, 16, 875–889.  803 <a href="https://doi.org/10.1130/GES02179.1">https://doi.org/10.1130/GES02179.1</a>, 2020.</a></p> <p>804 <a href="https://doi.org/10.1007/s00024-009-0511-4">de Jossineau, G., &amp; Aydin, A.: Segmentation along strike-slip faults revisited. <i>Pure and Applied  805 Geophysics</i>, 166(10–11), 1575–1594. <a href="https://doi.org/10.1007/s00024-009-0511-4">https://doi.org/10.1007/s00024-009-0511-4</a>, 2009.</a></p> <p>806 <a href="https://doi.org/10.1029/2011gl047849">DeDontney, N., Rice, J. R., &amp; Dmowska, R.: Influence of material contrast on fault branching behavior:  807 BImATERIAL BRANCHING. <i>Geophys. Res. Lett.</i> 38(14).  808 <a href="https://doi.org/10.1029/2011gl047849">https://doi.org/10.1029/2011gl047849</a>, 2011.</a></p> <p>809</p> <p>810 <a href="https://doi.org/10.1007/bf00875726">Deng, Q., Wu, D., Zhang, P., &amp; Chen, S.: Structure and deformational character of strike-slip fault zones.  811 <i>Pure and Applied Geophysics</i>, 124(1–2), 203–223. <a href="https://doi.org/10.1007/bf00875726">https://doi.org/10.1007/bf00875726</a>, 1986.</a></p> <p>812 <a href="https://doi.org/10.1016/j.tecto.2016.10.023">Díez-Fernández, R., Pereira, M.F.: Extensional orogenic collapse captured by strike-slip tectonics:  813 Constraints from structural geology and UPb geochronology of the Pinhel shear zone (Variscan  814 orogen, Iberian Massif). <i>Tectonophysics</i> 691, 290–310.  815 <a href="https://doi.org/10.1016/j.tecto.2016.10.023">https://doi.org/10.1016/j.tecto.2016.10.023</a>, 2016.</a></p> <p>816</p> <p>817 <a href="https://doi.org/10.1016/j.jsg.2012.05.030">Dooley, T. P., &amp; Schreurs, G.: Analogue modelling of intraplate strike-slip tectonics: A review and new  818 experimental results. <i>Tectonophysics</i>, 574–575, 1–71.  819 <a href="https://doi.org/10.1016/j.jsg.2012.05.030">https://doi.org/10.1016/j.jsg.2012.05.030</a>, 2012.</a></p> <p>820 <a href="https://doi.org/10.1029/95jb01574">Du, Y., &amp; Aydin, A.: Shear fracture patterns and connectivity at geometric complexities along strike-slip  821 faults. <i>Journal of Geophysical ResearchJ. Geophys. Res.</i>, 100(B9), 18093–18102.  822 <a href="https://doi.org/10.1029/95jb01574">https://doi.org/10.1029/95jb01574</a>, 1995.</a></p> <p>823 <a href="https://doi.org/10.1016/j.tecto.2004.05.005">Fernández, M., Marzán, I., &amp; Torne, M.: Lithospheric transition from the Variscan Iberian Massif to the  824 Jurassic oceanic crust of the Central Atlantic. <i>Tectonophysics</i>, 386(1–2), 97–115.  825 <a href="https://doi.org/10.1016/j.tecto.2004.05.005">https://doi.org/10.1016/j.tecto.2004.05.005</a>, 2004.</a></p> <p>826 <a href="https://doi.org/10.1016/j.precamres.2021.106365">Gabrielsen, R. H., Giannenas, P. A., Sokoutis, D., Willingshofer, E., Hassaan, M., &amp; Faleide, J. I.:  827 Analogue experiments on releasing and restraining bends and their application to the study of the</a></p>	<p><b>Con formato:</b> Espacio Después: 0 pto, Dividir palabras</p> <p><b>Con formato:</b> Fuente: Sin Cursiva</p> <p><b>Con formato:</b> Fuente: (Predeterminada) Times New Roman, 10 pto, Inglés (Estados Unidos)</p> <p><b>Con formato:</b> Inglés (Estados Unidos)</p> <p><b>Con formato:</b> Inglés (Estados Unidos)</p> <p><b>Con formato:</b> Inglés (Estados Unidos)</p> <p><b>Con formato:</b> Fuente: Sin Cursiva</p> <p><b>Con formato:</b> Fuente: (Predeterminada) Times New Roman, 10 pto, Inglés (Estados Unidos)</p> <p><b>Con formato:</b> Fuente de párrafo predeter., Fuente: (Predeterminada) +Cuerpo (Calibri), 11 pto, Inglés (Reino Unido)</p> <p><b>Con formato:</b> Inglés (Estados Unidos)</p> <p><b>Con formato:</b> Inglés (Estados Unidos)</p> <p><b>Con formato:</b> Fuente: (Predeterminada) Times New Roman, 10 pto, Inglés (Estados Unidos)</p> <p><b>Con formato:</b> Fuente de párrafo predeter., Fuente: (Predeterminada) +Cuerpo (Calibri), 11 pto, Inglés (Reino Unido)</p> <p><b>Con formato:</b> Sin subrayado, Color de fuente: Automático</p> <p><b>Con formato</b> ...</p> <p><b>Con formato:</b> Espacio Después: 0 pto</p> <p><b>Con formato</b> ...</p> <p><b>Con formato</b> ...</p> <p><b>Con formato</b> ...</p> <p><b>Con formato</b> ...</p> <p><b>Con formato</b> ...</p> <p><b>Con formato</b> ...</p> <p><b>Con formato</b> ...</p> <p><b>Con formato</b> ...</p> <p><b>Con formato</b> ...</p> <p><b>Con formato</b> ...</p> <p><b>Con formato</b> ...</p> <p><b>Con formato:</b> Espacio Después: 0 pto</p> <p><b>Con formato</b> ...</p> <p><b>Con formato</b> ...</p> <p><b>Con formato</b> ...</p> <p><b>Con formato</b> ...</p> <p><b>Con formato</b> ...</p> <p><b>Con formato</b> ...</p> <p><b>Con formato:</b> Fuente: Sin Cursiva</p> <p><b>Con formato</b> ...</p> <p><b>Con formato</b> ...</p>
--	--

828 Barents Shear Margin. *Solid Earth*, 14(9), 961–983. <https://doi.org/10.5194/se-14-961-2023>,  
829 2023

830 Gamond, J.F.: Displacement features associated with fault zones: a comparison between observed examples  
831 and experimental models. *Journal of Structural Geology*. *J. Struct. Geol.*, 5, 33–45, 1983.

832 Gapais, D., Fiquet, G., & Cobbold, P. R.: Slip system domains, 3. New insights in fault kinematics from  
833 plane-strain sandbox experiments. *Tectonophysics*, 188(1–2), 143–157.  
834 [https://doi.org/10.1016/0040-1951\(91\)90320-r](https://doi.org/10.1016/0040-1951(91)90320-r), 1991.

835 Garfunkel, Z., & Ron, H.: Block rotation and deformation by strike-slip faults: 2. The properties of a type  
836 of macroscopic discontinuous deformation. *Journal of Geophysical Research*, 90(B10), 8589–8602.  
837 <https://doi.org/10.1029/jb090i10p08589>, 1985.

838 Gomes, A. S., Rosas, F. M., Duarte, J. C., Schellart, W. P., Almeida, J., Tomás, R., & Strak, V.: Analogue  
839 modelling of brittle shear zone propagation across upper crustal morpho-rheological  
840 heterogeneities. *J. Struct. Geol., Journal of Structural Geology*, 126, 175–197.  
841 <https://doi.org/10.1016/j.jsg.2019.06.004>, 2019.

842 Gutiérrez-Alonso, G., Collins, A. S., Fernández-Suárez, J., Pastor Galán, D., González-Clavijo, E.,  
843 Jourdan, F., Weil, A. B., & Johnston, S. T.: Dating of lithospheric buckling: 40Ar/39Ar ages of  
844 syn-orocline strike-slip shear zones in northwestern Iberia. *Tectonophysics*, 643, 44–54.  
845 <https://doi.org/10.1016/j.tecto.2014.12.009>, 2015.

846 Harris, R.A., Day, S.M.: Dynamic 3D simulation of earthquakes on en echelon faults. *Geophysical*  
847 *Research Letters*. *Geophys. Res. Lett.*, 26, 2089–2092, 1999.

848 Hatem, A. E., Cooke, M. L., & Toeneboehn, K.: Strain localization and evolving kinematic efficiency of  
849 initiating strike-slip faults within wet kaolin experiments. *J. Struct. Geol.*, 101, 96–108.  
850 <https://doi.org/10.1016/j.jsg.2017.06.011>, 2017.

851 Hatem, A. E., Cooke, M. L., & Toeneboehn, K.: Strain localization and evolving kinematic efficiency of  
852 initiating strike-slip faults within wet kaolin experiments. *J. Struct. Geol.*, 101, 96–108.  
853 <https://doi.org/10.1016/j.jsg.2017.06.011>, 2017.

854

855 Hubbert, M. K.: Theory of scale models as applied to the study of geologic structures. *The Geological*  
856 *Society of America Bulletin*, 48(10), 1459–1520. <https://doi.org/10.1130/GSAB-48-1459>,  
857 1937.

858 Kavyani Sadr, K., Rahimi, B., Khatib, M.M., Kim, Y. S.: Assessment of open spaces related to Riedel  
859 shears dip effect in brittle shear zones. *J. Struct. Geol.* 154, 104486  
860 <https://doi.org/10.1016/j.jsg.2021.104486>, 2022.

861 Kim, Y., Peacock, D.C.P., Sanderson, D.J.: Fault damage zones. *J. Struct. Geol., Journal of Structural*  
862 *Geology* 26, 503–517, 2004.

863 Kirkland, C. L., Alsop, G. I., & Prave, A. R.: The brittle evolution of a major strike-slip fault associated  
864 with granite emplacement: a case study of the Leannan Fault, NW Ireland. *Journal of the Geological*  
865 *Society*. *J. Geol. Soc.*, 165(1), 341–352. <https://doi.org/10.1144/0016-76492007-064>, 2008.

866 Lefevre, M., Souloumiac, P., Cubas, N., & Klinger, Y.: Experimental evidence for crustal control over  
867 seismic fault segmentation. *Geology*, 48(8), 844–848. <https://doi.org/10.1130/g47115.1>, 2020.

868 Livio, F. A., Ferrario, M. F., Frigerio, C., Zerboni, A., & Michetti, A. M.: Variable fault tip propagation  
869 rates affected by near-surface lithology and implications for fault displacement hazard assessment.  
870 *Journal of Structural Geology*, 130(103914), 103914.  
871 <https://doi.org/10.1016/j.jsg.2019.103914>, 2020.

872 Mair, K., Frye, K.M., Marone, C.: Influence of grain characteristics on the friction of granular shear zones.  
873 *Journal of Geophysical Research*. *J. Geophys. Res.*, 107 (B10), 4/1-4/9, 2002.

874 Matte, P.: Accretionary history and crustal evolution of the Variscan belt in Western  
875 Europe. *Tectonophysics*, 196(3–4), 309–337. [https://doi.org/10.1016/0040-1951\(91\)90328-](https://doi.org/10.1016/0040-1951(91)90328-p)  
876 [p](https://doi.org/10.1016/0040-1951(91)90328-p).1991.

877 Martel, S.J., Peterson Jr., J.E.: Interdisciplinary characterization of fracture systems at the US/BK site,  
878 Grimsel Laboratory, Switzerland. *International Journal of Rock Mechanics and Mining Science and*  
879 *Geomechanical Abstracts* 28, 259–323, 1991.

880 Martínez Catalán, J. R., Arenas, R., Díaz García, F., & Abati, J.: Variscan accretionary complex of  
881 northwest Iberia: Terrane correlation and succession of tectonothermal events. *Geology*, 25(12),  
882 1103. [https://doi.org/10.1130/0091-7613\(1997\)025<1103:vaconi>2.3.co;2](https://doi.org/10.1130/0091-7613(1997)025<1103:vaconi>2.3.co;2), 1997

883

- Con formato: Fuente: Sin Cursiva
- Con formato: Fuente: Sin Cursiva
- Con formato: Fuente: (Predeterminada) Times New Roman, 10 pto, Inglés (Estados Unidos)
- Con formato: Espacio Después: 0 pto
- Con formato: Sin subrayado, Color de fuente: Automático
- Con formato: Fuente: Sin Cursiva, Sin subrayado, Color de fuente: Automático
- Con formato: Sin subrayado, Color de fuente: Automático
- Con formato: Fuente: Sin Cursiva, Sin subrayado, Color de fuente: Automático
- Con formato: Sin subrayado, Color de fuente: Automático
- Con formato: Fuente: (Predeterminada) Times New Roman, 10 pto, Inglés (Estados Unidos)
- Con formato: Sin subrayado, Color de fuente: Automático
- Con formato: Fuente: Sin Cursiva
- Con formato: Fuente: (Predeterminada) Times New Roman, 10 pto, Inglés (Estados Unidos)
- Con formato: Fuente: (Predeterminada) Times New Roman, 10 pto, Inglés (Estados Unidos)
- Con formato: Fuente: (Predeterminada) Times New Roman, 10 pto, Inglés (Estados Unidos)
- Con formato: Fuente: (Predeterminada) Times New Roman, 10 pto, Inglés (Estados Unidos)
- Con formato: Fuente: (Predeterminada) Times New Roman, 10 pto, Inglés (Estados Unidos)
- Con formato: Fuente: (Predeterminada) Times New Roman, 10 pto, Inglés (Estados Unidos)
- Con formato: Fuente: Sin Cursiva
- Con formato: Fuente: Sin Cursiva
- Con formato: Fuente: (Predeterminada) Times New Roman, 10 pto, Inglés (Estados Unidos)

884 Martínez Catalán, J.R.: The Central Iberian arc, an orocline centered in the Iberian Massif and some  
885 implications for the Variscan belt. *Int. J. Earth Sci.* 101, 1299–1314.  
886 <https://doi.org/10.1007/s00531-011-0715-6>, 2012.

887 Martín-González, F., Heredia, N.: Geometry, structures and evolution of the western termination of the  
888 Alpine-Pyrenean Orogen reliefs (NW Iberian Peninsula). *J. Iber. Geol.* 37, 103–120.  
889 [https://doi.org/10.5209/rev\\_JIGE.2011.v37.n2.1](https://doi.org/10.5209/rev_JIGE.2011.v37.n2.1), 2011.

890 Martín-González, F., Barbero, L., Capote, R., Heredia, N., & Gallastegui, G.: Interaction of two successive  
891 Alpine deformation fronts: constraints from low-temperature thermochronology and structural  
892 mapping (NW Iberian Peninsula). *International Journal of Earth Sciences/Int. J. Earth Sci.* 101(5),  
893 1331–1342. <https://doi.org/10.1007/s00531-011-0712-9>, 2012.

894 [Matte, P.: Accretionary history and crustal evolution of the Variscan belt in Western  
895 Europe. \*Tectonophysics\*, 196\(3–4\), 309–337. \[https://doi.org/10.1016/0040-1951\\(91\\)90328-  
896 p\]\(https://doi.org/10.1016/0040-1951\(91\)90328-p\), 1991.](https://doi.org/10.1016/0040-1951(91)90328-p)

897 [Misra, S., Mandal, N., Chakraborty, C.: Formation of Riedel shear fractures in granular materials: Findings  
898 from analogue shear experiments and theoretical analyses. \*Tectonophysics\* 471, 253–259.  
899 <https://doi.org/10.1016/j.tecto.2009.02.017>, 2009](https://doi.org/10.1016/j.tecto.2009.02.017)

900 Moore, J. D. P., & Parsons, B.: Scaling of viscous shear zones with depth-dependent viscosity and power-  
901 law stress–strain-rate dependence. *Geophysical Journal International/Geophys. J. Int.* 202(1), 242–  
902 260. <https://doi.org/10.1093/gji/ggv143>, 2015.

903 Myers, R., Aydin, A.: The evolution of faults formed by shearing across joint zones in sandstone. *Journal  
904 of Structural Geology/J. Struct. Geol.* 26, 947–966, 2004.

905 Nicholson, C., Seeber, L., Williams, P. and Sykes, L.R.: Seismic evidence for conjugate slip and block  
906 rotation within the San Andreas fault system, Southern California. *Tectonics*, 5: 629–648, 1986

907 Odling, N.E., Harris, S.D., Knipe, R.J.: Permeability scaling properties of fault damage zones in siliclastic  
908 rocks. *J. Struct. Geol., Journal of Structural Geology* 26, 1727–1747, 2004.

909 Panien, M., Schreurs, G., & Pfiffner, A.: Mechanical behaviour of granular materials used in analogue  
910 modelling: insights from grain characterisation, ring-shear tests and analogue experiments. *J. Struct.  
911 Geol., Journal of Structural Geology*, 28(9), 1710–1724.  
912 <https://doi.org/10.1016/j.jsg.2006.05.004>, 2006.

913 Peacock, D.C.P., Sanderson, D.J.: Displacement, segment linkage and relay ramps in normal fault zones.  
914 *J. Struct. Geol., Journal of Structural Geology* 13, 721–733, 1991.

915 Peacock, D. C. P., & Sanderson, D. J.: Effects of layering and anisotropy on fault geometry. *Journal of the  
916 Geological Society–J. Geol. Soc.*, 149(5), 793–802. <https://doi.org/10.1144/gsjgs.149.5.0793>,  
917 1992.

918 Petersen, M. D., Dawson, T. E., Chen, R., Cao, T., Wills, C. J., Schwartz, D. P., & Frankel, A. D.: Fault  
919 displacement hazard for strike-slip faults. *Bulletin of the Seismological Society of  
920 America*, 101(2), BSSA, 805–825. <https://doi.org/10.1785/0120100035>, 2011.

921 Preuss, S., Herrendörfer, R., Gerya, T., Ampuero, J.-P., & Dinther, Y.: Seismic and aseismic fault growth  
922 lead to different fault orientations. *Journal of Geophysical Research: Solid Earth/J. Geophys. Res.  
923 Solid Earth*, 124(8), 8867–8889. <https://doi.org/10.1029/2019jb017324>, 2019.

924 Ramberg, H.: Gravity, deformation and the Earth's crust: In theory, experiments and geological application  
925 (p. 452). Academic Press, 1981.

926 Richard, P.: Experiments on faulting in a two-layered cover sequence overlying a reactivated basement  
927 fault with oblique-slip. *J. Struct. Geol.* 13, 459–469, 1991.

928 Richard, P., Naylor, M.A., Koopman, A.: Experimental models of strike-slip tectonics. *Petroleum  
929 Geoscience/Pet. Geosci.* 1, 71–80, 1995.

930 Riedel, W.: *Zur Mechanik geologischer Brucherscheinungen*. *Centralblatt*. 1929.

931 Rispoli, R.: Stress fields about strike-slip faults inferred from stylolites and tension gashes. *Tectonophysics*  
932 75, 729–736, 1981.

933 Ron, H., Freund, R., Garfunkel, Z. and Nur, A.: Block rotation by strike slip faulting: structural and  
934 paleomagnetic evidence. *J. Geophys. Res.*, 89: 6256–6270, 1984.

Con formato: Sangría: Izquierda: 0 cm, Sangría francesa: 1 cm

Con formato: Fuente: (Predeterminada) Times New Roman, 10 pto, Inglés (Estados Unidos)

Con formato: Inglés (Estados Unidos)

Con formato: Fuente: (Predeterminada) Times New Roman, 10 pto, Inglés (Estados Unidos)

Con formato: Inglés (Estados Unidos)

Con formato: Fuente: Sin Cursiva

Con formato: Fuente de párrafo predeter., Fuente: (Predeterminada) +Cuerpo (Calibrí), 11 pto, Inglés (Reino Unido)

Código de campo cambiado

Con formato: Fuente: Sin Cursiva

Con formato: Fuente: Sin Cursiva

Con formato: Fuente: (Predeterminada) Times New Roman, 10 pto, Inglés (Estados Unidos)

Con formato: Inglés (Estados Unidos)

Con formato: Dividir palabras

Con formato: Fuente: Sin Cursiva

Con formato: Fuente: (Predeterminada) Times New Roman, 10 pto, Inglés (Estados Unidos)

Con formato: Fuente: Sin Cursiva

Con formato: Fuente: (Predeterminada) Times New Roman, 10 pto, Inglés (Estados Unidos)

Con formato: Espacio Después: 8 pto

Con formato: Sangría: Izquierda: 0 cm, Sangría francesa: 1 cm

Con formato: Espacio Después: 0 pto

Con formato: Fuente: Sin Cursiva

Con formato: Fuente: (Predeterminada) Times New Roman, 10 pto, Inglés (Estados Unidos)

Con formato: Fuente: (Predeterminada) Times New Roman, 10 pto, Inglés (Estados Unidos)

Con formato: Fuente: (Predeterminada) Times New Roman, 10 pto, Inglés (Estados Unidos)

Con formato: Espacio Después: 0 pto

Con formato: Espacio Después: 0 pto, Dividir palabras

Con formato: Dividir palabras

Con formato: Espacio Después: 0 pto

940 [Sammis, C. G., G. King, and R. Biegel. The kinematics of gouge deformation, \*Pure Appl. Geophys.\*, 125,](#)  
941 [777 – 812, 1987.](#)

942 [Schellart, W.P., Strak, V.: A review of analogue modelling of geodynamic processes: Approaches, scaling,](#)  
943 [materials and quantification, with an application to subduction experiments. \*J. Geodyn.\* 100, 7–32.](#)  
944 <https://doi.org/10.1016/j.jog.2016.03.009>, 2016.

945 Schmid, T., Schreurs, G. Warsitzka, M., & Rosenau, M.: Effect of sieving height on density and friction of  
946 brittle analogue material: Ring-shear test data of quartz sand used for analogue experiments in the Tectonic  
947 Modelling Lab of the University of Bern. GFZ Data Services.  
948 <https://doi.org/10.5880/fidgeo.2020.006>, 2020.

949 [Schmid, T. C., Schreurs, G., & Adam, J.: Rotational extension promotes coeval upper crustal brittle faulting](#)  
950 [and deep-seated rift-axis parallel flow: Dynamic coupling processes inferred from analog model](#)  
951 [experiments. \*Journal of Geophysical Research. Solid Earth\*, 127\(8\).](#)  
952 <https://doi.org/10.1029/2022jb024434>, 2022.

953 [Schmid, T. C., Brune, S., Glerum, A., & Schreurs, G.: Tectonic interactions during rift linkage: Insights](#)  
954 [from analog and numerical experiments. <https://doi.org/10.5194/egusphere-2022-1203>](#), 2023

955 [Scholz, C. H.: \*The Mechanics of Earthquakes and Faulting\*. Cambridge University Press, 2002.](#)

956 [Schreurs, G.: Experiments on strike-slip faulting and block rotation. \*Geology\*, 22\(6\), 567.](#)  
957 [https://doi.org/10.1130/0091-7613\(1994\)022<0567:eosfsa>2.3.co;2](https://doi.org/10.1130/0091-7613(1994)022<0567:eosfsa>2.3.co;2), 1994.

958 [Schreurs, G.: Structural analysis of the Schams nappes and adjacent tectonic units in the Penninic zone](#)  
959 [\(Grisons, SE-Switzerland\). ETH Zurich, 1991.](#)

960 [Schreurs, G.: Fault development and interaction in distributed strike-slip shear zones: an experimental](#)  
961 [approach. In: Storti, F., Holdsworth, R.E., Salvini, F. \(Eds.\), \*Intraplate Strike-slip Deformation\*](#)  
962 [Belts. \*Geol. Soc. Spec. Publ.\*, 210, 35–52, 2003](#)

963 [Scholz, C. H.: \*The Mechanics of Earthquakes and Faulting\*. Cambridge University Press, 2002.](#)

964 [Segall, P., & Pollard, D. D.: Nucleation and growth of strike-slip faults in granite. \*Journal of Geophysical\*](#)  
965 [Research](#), 88(B1), 555. <https://doi.org/10.1029/jb088ib01p00555>, 1983.

966 [Shaw, B.E., Dieterich, J.H.: Probabilities for jumping fault segment stepovers. \*Geophysical Research\*](#)  
967 [Letters-Geophys. Res. Lett.](#), 34, L01307. doi:10.1029/2006GL027980, 2007.

968 [Sibson, R.H.: Stopping of earthquake ruptures at dilational fault jogs. \*Nature\* 316, 248–251, 1985.](#)

969 [Stirling, M.W., Wesnousky, S.G., Shimazaki, K.: Fault trace complexity, cumulative slip, and the shape of](#)  
970 [the magnitude-frequency distribution for strike-slip faults: a global survey. \*Geophysical Journal\*](#)  
971 [International-Geophys. J. Int.](#), 124, 833–868, 1996.

972 [Sylvester, A.G.: Strike-slip faults. \*Geol. Soc. Am. Bull.\* 100, 1666–1703. \[https://doi.org/10.1130/0016-\]\(https://doi.org/10.1130/0016-7606\(1988\)1002.3.CO;2\)  
973 \[7606\\(1988\\)1002.3.CO;2\]\(#\), 1988.](#)

974 [Vegas, R., Vicente Muñoz, G., Muñoz Martín, A., & Palomino, R.: Los corredores de fallas de Régua-](#)  
975 [Verin y Vilarica: Zonas de transferencia de la deformación intraplaca en la Península Ibérica, 2004](#)

976 [Veludo, I., Dias, N. A., Fonseca, P. E., Matias, L., Carrilho, F., Haberland, C., & Villaseñor, A.: Crustal](#)  
977 [seismic structure beneath Portugal and southern Galicia \(Western Iberia\) and the role of Variscan](#)  
978 [inheritance. \*Tectonophysics\*, 717, 645–664. <https://doi.org/10.1016/j.tecto.2017.08.018>.](#)  
979 [2017](#)

980 [Venâncio, M. B., & da Silva, F. C. A.: Structures evolution along strike-slip fault zones: The role of](#)  
981 [rheology revealed by PIV analysis of analog modeling. \*Tectonophysics\*, 229764, 229764.](#)  
982 <https://doi.org/10.1016/j.tecto.2023.229764>, 2023.

983 [Vergés, J., Kullberg, J. C., Casas-Sainz, A., de Vicente, G., Duarte, L. V., Fernández, M., Gómez, J. J.,](#)  
984 [Gómez-Pugnaire, M. T., Jabaloy Sánchez, A., López-Gómez, J., Macchiavelli, C., Martín-Algarra,](#)  
985 [A., Martín-Chivelet, J., Muñoz, J. A., Quesada, C., Terrinha, P., Torné, M., & Vegas, R.: An](#)  
986 [introduction to the alpine cycle in Iberia. En \*The Geology of Iberia: A Geodynamic Approach\* \(pp.](#)  
987 [1–14\). Springer International Publishing, 2019](#)

988 [Visage, S., Souloumiac, P., Cubas, N., Maillot, B., Antoine, S., Delorme, A., & Klinger, Y.: Evolution of](#)  
989 [the off-fault deformation of strike-slip faults in a sand-box](#)  
990 [experiment. \*Tectonophysics\*, 847\(229704\), 229704.](#)  
991 <https://doi.org/10.1016/j.tecto.2023.229704>, 2023.

992 [Viola, G., Odone, F., Manektelow, N.S.: Analogue modelling of reverse fault reactivation in strike-slip](#)  
993 [and transpressive regimes: application to the Giudicarie fault system, Italian Eastern Alps. \*J. Struct.\*](#)  
994 [Geol.](#) 36, 401–418. <https://doi.org/10.1016/j.jsg.2003.08.014>, 2004.

995 [Wesnousky, S.G.: Seismological and structural evolution of strike-slip faults. \*Nature\* 335, 340–342, 1988.](#)

996 [Wesnousky, S.G.: Predicting the endpoints of earthquake ruptures. \*Nature\* 444, 358–360, 2006.](#)

- Con formato: Inglés (Estados Unidos)
- Con formato: Sin subrayado, Color de fuente: Automático
- Con formato: Espacio Después: 0 pto
- Con formato: Fuente: (Predeterminada) Times New Roman, 10 pto, Inglés (Estados Unidos)
- Con formato: Sin subrayado, Color de fuente: Automático
- Con formato: Sin subrayado, Color de fuente: Automático
- Con formato: Espacio Después: 0 pto
- Con formato: Sin subrayado, Color de fuente: Automático, Sin Tachado
- Con formato: Dividir palabras
- Con formato: Fuente: Sin Cursiva
- Con formato: Sin subrayado, Color de fuente: Automático
- Con formato: Fuente: Sin Cursiva, Sin subrayado, Color de fuente: Automático
- Con formato: Sin subrayado, Color de fuente: Automático
- Con formato: Fuente: Sin Cursiva, Sin subrayado, Color de fuente: Automático
- Con formato: Sin subrayado, Color de fuente: Automático
- Con formato: Fuente: Sin Cursiva, Sin subrayado, Color de fuente: Automático
- Con formato: Fuente: (Predeterminada) Times New Roman, 10 pto, Inglés (Estados Unidos)
- Con formato: Sin subrayado, Color de fuente: Automático
- Con formato: Fuente: Sin Cursiva, Sin subrayado, Color de fuente: Automático
- Con formato: Sin subrayado, Color de fuente: Automático
- Con formato: Inglés (Estados Unidos)
- Con formato: Espacio Después: 0 pto
- Con formato: Espacio Después: 0 pto
- Con formato: Inglés (Estados Unidos)
- Con formato: Fuente: Sin Cursiva, Inglés (Estados Unidos)
- Con formato: Inglés (Estados Unidos)
- Con formato: Fuente: (Predeterminada) Times New Roman, 10 pto, Inglés (Estados Unidos)
- Con formato: Fuente: (Predeterminada) Times New Roman, 10 pto, Inglés (Estados Unidos)
- Con formato: Fuente: Sin Cursiva
- Con formato: Fuente: Sin Cursiva
- Con formato: Fuente: (Predeterminada) Times New Roman, 10 pto, Inglés (Estados Unidos)
- Con formato: Espacio Después: 0 pto

998 ~~Westerweel, J., Scarano, F.: Universal outlier detection for PIV data. Experiments in fluids 39,~~  
999 ~~1096-1100, 2005.~~  
1000 ~~Zhang, X., & Sagiya, T.: Shear strain concentration mechanism in the lower crust below an intraplate strike-~~  
1001 ~~slip fault based on rheological laws of rocks. EPS, 69(1). [0668-5](https://doi.org/10.1186/s40623-017-</a></del><br/>
1002 <del><a href=), 2017.~~  
1003 ~~Zwaan, F., Schreurs, G., Ritter, M., Santimano, T., & Rosenau, M.: Rheology of PDMS-corundum sand~~  
1004 ~~mixtures from the Tectonic Modelling Lab of the University of Bern (CH). V. 1. GFZ data Services.~~  
1005 ~~<https://doi.org/10.5880/fdgeo.2018.023>, 2018.~~  
1006 ~~Zwaan, F., Schreurs, G., Gentzmann, R., Warsitzka, M. & Rosenau, M. Ring shear test data of quartz sand~~  
1007 ~~from the Tectonic Modelling Lab of the University of Bern (CH). GFZ Data Services.~~  
1008 ~~<http://doi.org/10.5880/fdgeo.2018.028>~~  
1009 ~~Zwaan, F., Schreurs, G., Madritsch, H., & Herwegh, M.: Influence of rheologically weak layers on fault~~  
1010 ~~architecture: insights from analogue models in the context of the Northern Alpine Foreland Basin.~~  
1011 ~~Swiss Journal of Geosciences, 115(1). <https://doi.org/10.1186/s00015-022-00427-8>, 2022.~~  
1012

**Con formato:** Fuente de párrafo predeter., Fuente: (Predeterminada) +Cuerpo (Calibri), 11 pto, Inglés (Reino Unido)

**Con formato:** Fuente: Sin Cursiva

**Con formato:** Fuente: Sin Cursiva

**Con formato:** Fuente: (Predeterminada) Times New Roman, 10 pto, Inglés (Estados Unidos)

**Con formato:** Inglés (Estados Unidos)

**Con formato:** Sin subrayado, Color de fuente: Automático

**Con formato:** Fuente de párrafo predeter., Fuente: (Predeterminada) +Cuerpo (Calibri), 11 pto, Inglés (Reino Unido)